FACULTY
OF MATHEMATICS
AND PHYSICS
Charles University

MASTER THESIS

Jiří Jechumtál

Study of spin dynamics in magnetic metals using terahertz and optical spectroscopy

Department of Chemical Physics and Optics

Supervisor of the master thesis: RNDr. Lukáš Nádvorník, Ph.D.
Study programme: Physics
Study branch: Optics and optoelectronics

Prague 2022

I declare that I carried out this master thesis independently, and only with the cited sources, literature and other professional sources. It has not been used to obtain another or the same degree.

I understand that my work relates to the rights and obligations under the Act No. 121/2000 Sb., the Copyright Act, as amended, in particular the fact that the Charles University has the right to conclude a license agreement on the use of this work as a school work pursuant to Section 60 subsection 1 of the Copyright Act.

In .... date ....
Author's signature

I would like to thank to my master thesis supervisor Dr. Lukáš Nádvorník for professional guidance and for help and advice in preparing this work. Many thanks also go to the people who prepared the experiments in the laboratories, so we could realize our experiments. In the Berlin Laboratory at the Freie Universität at the Fritz Haber Institute of the Max Plack Society, especially to its head Prof. Tobias Kampfrath and also PhD student Oliver Güeckstock, in the Prague laboratory espetially to my collegue Mgr. Peter Kubaščík.

Title: Study of spin dynamics in magnetic metals using terahertz and optical spectroscopy

Author: Jiří Jechumtál, Department of Chemical Physics and Optics

Supervisor: RNDr. Lukáš Nádvorník, Ph.D., Department of Chemical Physics and Optics

Abstract: Understanding of the ultrafast spin dynamics is essential for application and further development of new spintronic devices. The ultrafast spintronics is a promising path towards faster and less energetically demanding technologies comparing to current electronics. Recent studies have reported on a novel possibility of investigation of ultrafast out-of-plane spin transport using the technique of spintronic generation of terahertz (THz) pulses. This work focuses on determining the nature of out-of-plane spin transfer in spintronic THz emitters by direct experimental quantification of the spin current relaxation length and the speed of spin propagation. Our results suggest that the ultrafast spin currents are of the ballistic nature and the spin current relaxation time is limited by the scaterring time and the relaxation length by the mean free path. Another recentely published method, also used in this work, is the the contactless THz measurement of anisotropic magnetoresistance (AMR). In a thin layer of cobalt-iron, we demonstrate that the AMR, a central phenomenon commonly used in the antiferromagnetic spintronics to read the state of magnetic order, can be investigated by the THz spectroscopy even if dominated by the crystalline term. We complement the study by a spectral analysis of the crystalline AMR.

Keywords: spin dymanics, ultrafast spintronics, terahertz spectroscopy

Contents

Introduction **3**

1 Theory **5**

1.1 Spintronic emitters of THz radiation 5
1.1.1 Introduction to spin and its interactions 5
1.1.2 Spin Hall effect 6
1.1.3 Spintronic emission of THz pulses 8
1.2 Ultrafast processes in spintronic emitters 9
1.2.1 Ultrafast demagnetization 9
1.2.2 Origins of ultrafast spin transport 10
1.3 Electron and spin transports 11
1.3.1 Drude model of diffusive transport 11
1.3.2 Ballistic transport 12
1.3.3 Relaxations of spin currents 13
1.4 Anisotropic magnetoresistence 14
1.4.1 Origins and symmetries of AMR 14
1.4.2 THz investigation of AMR 16
1.4.3 AMR in cobalt-iron 16

2 Methods **18**

2.1 Experimental setups 18
2.1.1 Berlin and Prague setups 18
2.1.2 Detection and evaluation of THz pulses 20
2.2 Conductivity measured by THz radiation 22
2.3 Parameters of STE affecting THz emission 23
2.4 THz measurement of AMR 24
2.5 Samples 26
2.5.1 Design of samples for THz emission experiment 26
2.5.2 Fabrication of samples for THz emission experiment 27
2.5.3 Fabrication of samples for THz AMR measurement 28
2.6 Gaussian beams and their propagation 28

3 Experiment **30**

3.1 Out-of-plane spin current: Spin relaxation 30
3.1.1 Measurement of optical absorption 30
3.1.2 THz measurement of conductivity 32
3.1.3 Spin current relaxation length from THz amplitudes 35
3.1.4 Robustness of results 38
3.2 Out-of-plane spin current: Speed of propagation 40
3.2.1 Evaluation of THz waveform's shifts 40
3.2.2 Speed of electron transport in STE 44
3.3 Out-of-plane spin current: Relaxation time 48
3.4 Out-of-plane spin current: Spectral filtering in copper 49
3.5 Inplane spin current: THz crystalline AMR 51

3.5.1 First observation: magnetic-field-dependent modulation of THz transmitance 52
3.5.2 Contrast of AMR vs. crystallographic orientation: cross-crystalline AMR 53
3.5.3 Spectral dependence of intrinsic AMR 55
3.5.4 Discussion on THz measurement of AMR 56

Conclusion **58**

Bibliography **60**

List of Figures **65**

Introduction

In this master thesis, we will study ultrafast (i.e., subpicosecond) spin transport in metals and magnetic materials using terahertz time-domain spectroscopy (TTDS).

Using not only the charge of the electron, but also its inner magnetic moment - spin, is the corner stone of the spintronics [1, 2, 3]. Today's electronics is already approaching its limits in terms of miniaturization and speeding up and the self-fulfilling Moore's law, speaking about multiplication of the density of transistors on the area in an integrated circuit, is already slowing down [4]. Spintronics is one of the ways how the mankind is dealing with the ongoing need for speeding up our technologies, but also making them less energetically demanding [5]. In today's technologies, spintronic effects such as giant or tunelling magnetoresistence in reading heads of hard drive discs [6] or in magnetic random acces memories [7, 8] are allready used. But for development of a new generation of ultrafast spintronic devices and technologies, it is essential to understand the fundamental physiscs of ultrafast spin dynamics. This is the motivation for us to study the spin polarized electron transport in metal nanostructures in this work.

The research method used in this thesis is the TTDS. It is an original method introduced in second half of the 20^{th} century with development of generation of ultrashort optical pulses [9], [10]. Terahertz (THz) radiation is the electromagnetic radiation spanning over frequencies from 0.1 to 30 THz, i.e., wavelengths from units of milimeters to micrometers. By TTDS, it is usually meant the method where picosecond-long THz pulses are generated by ultrashort (tens of femtoseconds) optical pulses which are later also used for the optical detection of THz pulses. The method is unique by its ability of reconstructing directly the electric field including its phase, not only intensity, which brings the possibility of condensed matter research such as direct measurement of complex refractive index, conductivity, electric transient currents and polarization and also the spectral dependence of these quantities [9]. The time resolution, especially in case of higher THz frequencies, can reach even subpicosecond scales which is the motivation for using this method for studying ultrafast processes by THz emission spectroscopy [11] or by THz transmition spectroscopy.

In this work, we will employ the new spintronic THz sources introduced by Seifert *et al.* in 2016 [12] which use the inverse spin Hall effect [13, 14] of photoexcited spin-polarized electrons. The emitters are typically constructed from two only few nanometers thick ferromagnetic and nonmagnetic metallic layers. The big advatage is that they are sources of strong THz radiation up to 30 THz [12] and, as they are using spintronic effects, they can be used not only as the source of THz radiation but also as a research tool in spintronics and spin dynamics. That includes ultrafast processes (as the photo-excited spin polarized electrons have to be transported across the metal layers) so these emitters can also be used for studying of the ultrafast demagnetization and ultrafast out-of-plane spin transport [15]. Another bonus is the fact that these emitters were studied in my bachelor thesis [16], so I have good experiences with their properties.

The first goal of this thesis is to study the ultrafast out-of-plane spin polarized electron transport in copper using the principle of THz emission from spintronic emitters combined with additional copper layer. From evaluation of emitted THz waveforms, we want to study the spin current relaxation length in copper, similar to Seifert *et al.* [11], and, more importantly, the speed of spin-polarized electrons in copper. Having these two quantities, we can reconstruct also the spin current relaxation time and ultimately answer the question about predictions of out-of-plane spin polarized electron transport in thin metal layers to be ballistic [17].

Another goal of this thesis is to study ultrafast inplane spin-dependent electron transport in cobalt-iron (CoFe) using transmission TTDS. We want to demonstrate the THz contactless measurement of anisotropic magnetoresistence (AMR) [18], previously measured in this material only using fully electrical methods by Zeng *et al.* [19]. CoFe is special for its huge crystalline part of AMR and this can be perfect opportunity to compare behavior of electrons from normal electric measurement with these excited by the THz radiation. As AMR in this material is quite unconventional, it can be also interesting to study the spectral changes in crystalline AMR depending on crystallographic orientation which can be also accessed by TTDS.

This work will be experimentally realized in two laboratories - the THz laboratory in Berlin at Freie Universität and at Fritz Harber institut of Max Planck Society in the group of prof. Thobias Kampfrath and the new laboratory of THz spintronics in Prague at Charles university, Faculty of Mathematics and Physics, department of Chemical Physics and Optics under Dr. Lukáš Nádvorník's supervision. The Berlin laboratory is perfectly prepared to THz measurements in higher THz frequencies and it is the place where the spintronic emitters were invented and optimized. So, it is the perfect place where to measure the first part of the work devoted to out-of-plane spin polarized electron transports. The Prague laboratory, on the other hand, is still in process of development. So, THz measurements of AMR can be perfect oportunity to demonstrate actual abilities of the laboratory. Moreover, AMR measurements do not need so high time resolution and they are perfectly doable also using lower THz frequencies which are currently available in Prague.

1. Theory

In theoretical part of this thesis we will briefly introduce spin and studied spintronic effects, ultrafast phenomenons and spin transport in out-of-plane direction studied using spintronic emission of THz pulses and in-plane electron transport for THz transmission experiments used for study of anisotropic magnetoresistance. The introductory section 1.1 and part of the section devoted to transports (1.3.1 and 1.3.3) cover the same issues as the theoretical sections in my bachelor's thesis [16] (written in Czech), but due to the consistency of the English text we do not refer there, but in an updated form we present this information again.

1.1 Spintronic emitters of THz radiation

For measurements included in this work, it is essential to undestand the spintronic emitter of THz radiation. It is allready an applied source of broadband THz radiation used in this thesis as a source for THz transmission experiments, but also a great bridge connecting the spintronic effects such as Spin Hall effect and spin transport in common, studied in this thesis, with THz emission.

1.1.1 Introduction to spin and its interactions

At the very begining, it is necessary to define spin. Spin is describing an internal magnetic moment that we assign to elementary particles. Specially for our theory, we have to focus on electron spin. In quantum mechanics electron spin is represented by the operator of spin momentum $\hat{\boldsymbol{S}} = \frac{\hbar}{2}\boldsymbol{\sigma}$, where $\boldsymbol{\sigma}$ is the vector of Pauli matrices [13]. Thanks to the algebra of Pauli matrices, it is easy to see that spin has just two own states in each directional projestion. Standardly, we are interested in the projection of spin into z-axis and we mark the two states symbolicaly by $|\uparrow>$ for the state $\begin{bmatrix}1\\0\end{bmatrix}$ and $|\downarrow>$ for the state $\begin{bmatrix}0\\1\end{bmatrix}$. [13] The magnetic momentum is then given by equation $\boldsymbol{\mu} = \frac{e}{m}\hat{\boldsymbol{S}}$, where e is the elementary charge and m is mass of the particle.

For understanding the interactions of spin, we have to consider the solution of Dirac equation up to the members $\approx \frac{1}{c^2}$. Then we will recieve the spin-orbit member of Hamiltonian as: [13]

$$\hat{H}_{SO} = \frac{e\hbar}{4mc^2}\boldsymbol{\sigma} \cdot (\boldsymbol{v} \times \boldsymbol{E}), \tag{1.1}$$

where $\boldsymbol{v}$ is the velocity of electron and $\boldsymbol{E}$ is the electric field. Considering the nonrelativistic Hamiltonian in magnetic field $H = \boldsymbol{\mu} \cdot \boldsymbol{B}$, we could intuitively see, that the member $\frac{1}{2c^2}(\boldsymbol{v} \times \boldsymbol{E})$ is just the relativistic transformation of magnetic field of charged particle moving with the velocity $\boldsymbol{v}$.

Now we have well defined spin and its interactional hamiltonian for a single particle. However for description of macroscopically obsevable effects there is a need to specify the spin properties of a larger statistical ensemble. For this purpose we itroduce spin polarization as: [13]

$$P = \frac{n^{\uparrow} - n^{\downarrow}}{n^{\uparrow} + n^{\downarrow}}, \tag{1.2}$$

where $n^{\uparrow\downarrow}$ reprezent the nuber of particles with projection of spin in examined direction $|\uparrow>$, or $|\downarrow>$. There are several options how to get locally spin-polarized material.

First, there are materials with their own internal magnetization caused by areas (named magnetic domains) where spins are in equilibrium oriented mainly in one direction - ferromagnets (FM). However nonmagnetic materials could be spin-polarized as well. In semiconductors, the spin polarization is standardly introduced, for example, by excitation with circularly polarized light.[20, 21]. In metals, the usual way is via the electrical spin injection which appears when electrical current is sent from a ferromagnet to a non-magnet or by spin-orbit effects, such as spin Hall effect, in uniquely non-magnetic (NM) materials. [14, 22, 23, 24].

However in both - ferromagnetic or nonmagnetic materials - the unbalanced spin polarization, no matter how created, relaxes to its original equilibrium state (non-zero in FM, zero in NM). There are several microscipic machanisms of relaxation including the spin-orbit interaction or interaction with external fields [13, 25] but, in general, we can describe them by the exponential relaxation equation [13]:

$$P_z(t) = P_{z0} e^{-t/\tau_s}, \tag{1.3}$$

where P_z is spin polarization in direction of z axis, P_{z0} is the original - unbalanced - value and τ_s is spin relaxation time. It is the value of the spin relaxation time that depends on the specific microscopic mechanisms.

As next step after definig the spin polarization, we have to introduce the spin current. We understand the term *spin current* as a shift of the spin polarization $P_{\hat{s}}$ with projection of spin $\hat{\boldsymbol{S}}$ through the material. The defining equation is [13, 25]

$$\boldsymbol{j_{\hat{s}}} = \boldsymbol{j_s} = P_{\hat{s}} \frac{\hbar}{2} \frac{\boldsymbol{j_c}}{e}, \tag{1.4}$$

where $\boldsymbol{j_c}$ is the charge current and e is the charge of electron. As indicated in equation, for simplicity further we write the index s instead of $\hat{s}$ and we automatically mean quantization in the natural direction of spin projection.

Like the spin polarization, the spin currents also relax due to various microscopic mechanisms. These mechanisms will be mentioned in the chapter devoted to electron and spin transport.

1.1.2 Spin Hall effect

After the introduction of spin, the form of its interaction and quantities describing the spin properties of larger systems, we could start with describing effects based on them. Specially for spintronic emiters of THz radiation, it is crucial to understand the Spin Hall effect (SHE) and its inverse counterpart - Inverse Spin

Hall effect (ISHE) [14]. As the name suggests, there is a big analogy to classical Hall effect.

Classical Hall effect describes formation of a transverse charge current in the sample through which a longitudinal charge current flows and which is inserted into an out-of-plane magnetic field. It is due to the Lorentz force, acting in the direction perpendicular to the magnetic field and the direction of the flow of electrons [26].

Spin Hall effect describes the flow of electrons (longitudinal charge current) in the sample, which is not inserted in an external magnetic field. But, as we know, the electrons holding the charge have also their spin. Therefore, due to the spin-orbit interaction during scattering on lattice atoms or impurities or other perturbations, electrons deflect in different directions according to their spin projection in the direction perpendicular to plane of motion and deflection. This leads, on a makcoscopic scale, to an accumulation of electrons with opposite projections of spins on the opposite sides of the conductor as you could see in Fig. 1.1 a) and b).[16] This means that, despite the fact that no perpendicular charge current flows through the sample, a perpendicular spin current is produced:

$$\boldsymbol{j_s} = \gamma(\hat{\boldsymbol{s}} \times \boldsymbol{j_c}), \tag{1.5}$$

where $\hat{\boldsymbol{s}}$ is a unit vector in direction of spin projection of the particle, $\boldsymbol{j_c}$ is the classical charge current density and γ is spin Hall angle - the coefficient reflecting the strength of the spin-orbit interaction typical for the given material.

As Fig. 1.1 c) suggests, this process can also be inversed. It means that the spin current excites the perpendicular charge current. Fig. 1.1 d) shows us the most common situation where the spin-polarized charge carriers cause both the SHE and ISHE by their flow through the material.

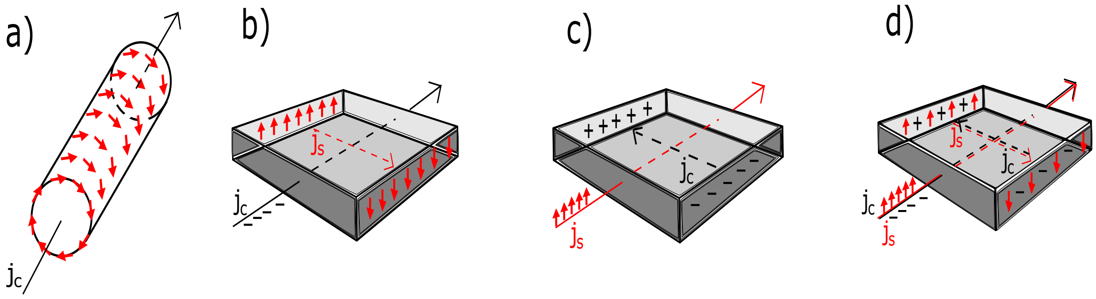

Figure 1.1: a) Formation of spin polarization at the edges of the conductor through which the current flows. b) SHE and the corresponding spin current j_s for pure charge current j_c, c) ISHE for pure spin current j_s, d) combination of SHE and ISHE in real cases. Taken from [16].

1.1.3 Spintronic emission of THz pulses

Now we have all necessary tools to describe the priciple of THz emision from spintronic emitter. Arrangement of emitters and description of phenomena that occur during the generation of THz pulses are based on previous work of German colleagues [12, 11, 23, 27, 28], and my bachelor's thesis [16].

As mentioned before, the time-resolved THz spectroscopy is a powerful research tool. The basic idea on which the spintronic emitter is based, is to use the ultrashort femtosecond laser pulses. Their envelope has approximately the Gaussian shape and contains the THz frequences. So, if ve have some process proportional to the intensity of exciting pulse, we could make use of these frequences. In case of spintronic emiters this process is a simple absorption.

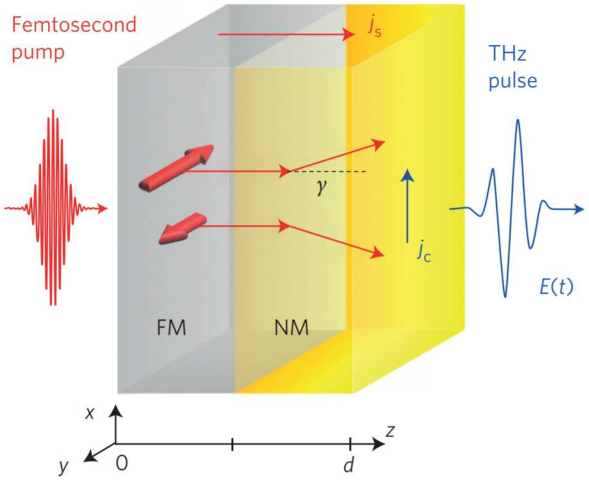

Figure 1.2: Scheme of spintronic emitter operation. Optical pulse propagating along the z axis hits the feromagnet layer (FM). Absorbed fotons excite electrons above the Fermi level. Thick red arrows represent the fact, that in magnetized ferromagnet there is a predominance of electrons with one orientetion of spin (along the negative direction of y axis). Thanks to the broken symetry of the bilayer a spin current is created associated with the transfer of excited, spin polarized charges to the non-magnetic metal (NM). Here, due to the ISHE, a charge current j_c is generated in the perpendicular direction which plays the role of a Hertzian dipole emitting the THz wave form on the right side. Taken from [12].

We will describe the whole process of creating of the THz puls in Fig. 1.2. First, the femtosecond laser pupm comes through the transparent substrate (glass or saphire - not shown in the figure, it would be on the negative half axis z) on the left side of the picture. It hits the only units of nanometer thick bilayer, and by its absorption it excites electrons in the whole stack. The electrons in FM are spin polarized (as it is represented by the thick red arrows) in the plane along the magnetization and because of the broken symetry of the bilayer (further discussed in the following section [15]), the electrons are flowing to NM. This causes the out-of-plane spin current j_s (thin red arrows in Fig. 1.2). In nonmagnetic layer, the perpendicular charge current j_c arises thanks to the ISHE whose size is related to

j_s through γ. This inplane charge current (represented by the blue arrow) works as a Hertzian dipole for the emitted THz pulse on the right side of the picture. Using mathematical symbols:

$$E_{THz} \propto j_c \propto j_s\gamma. \tag{1.6}$$

As it is obvious from the mechanism of the generation, the THz pulse is linearly polarized in perpedicular direction to the magnetization and it is possible to manipulate with the polarization easily only by changing the magnetization, for example by external magnetic field in the area of the emiter.

Looking at Eq. 1.6, we see that by analysis of emitted THz pulse we can study the dynamic of j_c (so also γj_s). Since it has already been demonstrated that ISHE has an immediate response to the stimulus (the SHE spectrum is flat up to frequencies of tens of THz) [29], we can get a good idea of the original ultrafast spin current j_s, which we will discuss in the next section.

1.2 Ultrafast processes in spintronic emitters

In order to gain a deeper understanding of the origin of processes and their dynamics in spintronic emitters, we must deal in more detail with the mechanism of spin current generation.

1.2.1 Ultrafast demagnetization

First, we would like to focus on the mechanism of ultrafast demagnetization (UDM). The term ”ultrafast” refers to processes that occur on picosecond and sub-picosecond time scales, which corresponds also to the frequency range of THz pulses. Previous works [30, 31, 32] have shown, that excitation of ferromagnetic layer leads to UDM in the layer.

To understand the dynamics of the process, we have to know a bit about the band structure of ferromagnets. The scheme of a specific band structure in a given ferromagnet is usually very complicated, but basically we only need to know the density of states (DOS) here. In most of the cases, it looks schematically like in Fig. 1.3 a) [15]. The DOS under the Fermi level is bigger for one projection of the spin (here $|\uparrow>$), than for the second (here $|\downarrow>$), but above the Fermi level the situation is reversed. Immediately after excitation by a laser pulse, the transient electron distribution can not be described by the Fermi-Dirac distribution (it is not yet thermalized). However, due to the fact that the excitation occurs mainly in electrons that were initially close to the Fermi level (i.e., $|\uparrow>$ due to the asymmetric DOS) and, in addition, since the DOS above original Fermi level is smaller for $|\uparrow>$, spin-up electrons are necessarily excited to higher energy levels than the spin-down electrons. That means the chemical potential $\mu^{\uparrow}$ is located higher in energy than $\mu^{\downarrow}$ as shown in Fig. 1.3 b).

In that situation, it means that the hotter electrons (that with higher energy) tend to have more interactions (electron-electron and electron-phonon), where they could exchange (and, therefore, flip) the spin state and get to the lower energies. Because the energy relaxation of all electronic ensemble to the original state is much slower, it means that, on the ultrafast time scale, the magnetization is decreasing [15, 33].

Because time change of magnetization necessarily induces an electromagnetic wave and the process is on the same time scale as THz pulses, it is no surprise, that an associated emission of THz radiation can be observed from a single FM layer.

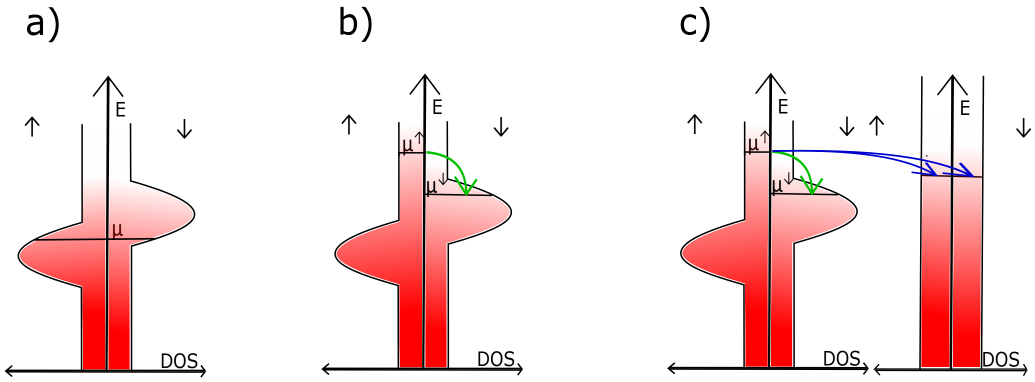

Figure 1.3: Scheme of ultrafast demagnetization proces. a) The scheme of DOS in FM, μ shows the Fermi level. b) The transient state of FM after excitation, green arrow represents the UDM process. c) Same situation as in b) in FM/NM bilayer, where also the UST represented by blue arrows is present.

1.2.2 Origins of ultrafast spin transport

As mentioned in section devoted to spintronic emiters, the process of THz pulse emission relies on the triggering of the spin current j_s from the magnetic to the nonmagnetic layer. However, the origin of j_s has remained a mystery since the discovery of the spintronic THz emission in 2016. Very recently, the work by R. Rouzegar *et al.*. [15] has shown the relation between the ultrafast spin transport (UST) and UDM. In particular, by comparing THz waveforms from single ferromagnetic layers with bilayers composed of the same ferromagnet and a nonmagnetic metal, they demonstrated that both processes have a completely same dynamics and that these are, basically, two names for the same phenomenon.

The basic idea could be illustrated again by considering the DOS in a FM/NM bilayer after the pulse excitation as shown in Fig. 1.3 c). As discussed before, after excitation of the ferromagnetic layer, we obtain an unbalanced distribution, where electons with spin |↑> reside on higher energies, i. e., higher $\mu^\uparrow$ than $\mu^\downarrow$. However, since a NM layer is attached to it, the process of UDM (equilibration of $\mu^\uparrow$ and $\mu^\downarrow$) is mediated also through a new relaxation channel: by the transport of spin-polarized electrons to the nonmagnetic layer (as indicated by blue arrows in fig. 1.3 c)).

From Fig. 1.3 and [15], it follows that j_s, which is directly proportional to j_c and emitted THz wave, is also directly proportional to the difference $\mu^\uparrow$ - $\mu^\downarrow$, or so-called spin voltage.

This result means that by measuring the emitted transient THz waveforms we obtain information not only about the UST but also the UDM dynamics itself. Although one of the aims of this work is to determine the nature of such created spin transport, we see that the obtained results can also provide information about a more complex overall problem.

1.3 Electron and spin transports

While the origin of the ultrafast current j_s has already been elucidated, there is still intense debate about the nature of such spin transport. Many observations have been made since the discovery of STE, suggesting that the distance over which the j_s contributes to j_c formation (and thus THz emission) is relatively localized to the depth of nm units from the interface [11, 12, 28, 34].

However, this is in a sharp contrast to common experience where spin diffusion transport lengths are one to two orders of magnitude longer [14]. Thus, some previous studies have hypothesized that the spin current is not diffusive in nature [27, 28, 15, 35]. This expectation is also supported by a theoretical model [17]. Verification of this hypothesis and decision on this problem is a central question of this thesis. In this section, we will prepare the starting points for the experimental part of the work.

There are several approaches how to describe the electron transport in materials. First, we introduce diffusive model described by classical Drude model [36] and the phenomenological parameters such as the conductivity. Then we introduce the ballistic model of electron transport and its specifics.

1.3.1 Drude model of diffusive transport

As already mentioned, the Drude model is a classical, nonrelativistic model describing the electron transport in metals. It works with macroscopic conductance σ, which we could measure using THz field as we explain in Methods section.

In this model, electrons in metal are approximated by ideal balls which behave like a particles of ideal gas and their only reaction is the flexible scaterring on spatially fixed positively charged lattice ions. Between the individual scattering events, only the applied external electric field acts on the particles and speeds them up. The greatest goal of this theory is the microscopic clarification of Ohm's law [36]:

$$\boldsymbol{j} = \frac{ne^2\tau}{m}\boldsymbol{E} = \sigma_0\boldsymbol{E}. \tag{1.7}$$

Here $\boldsymbol{j}$ is the charge density, $\boldsymbol{E}$ is the external electric field and σ_0 is the quasi-static (DC, "direct current") electrical conductivity expresed by the density of charge carriers n, the mean time between scaterrings τ and the charge of electron e.

Another achievement of the Drude model is the equation describing conductivity as a function of frequency ω of the alternating (AC) external field:

$$\sigma(\omega) = \frac{\sigma_0}{1 - i\omega\tau}, \tag{1.8}$$

where σ_0 is DC conductivity from the equation above.

The real part of frequency-dependent conductivity is a monotonically decreasing function and decreases the most at ω near τ^{-1} and at frequencies significantly lower it is almost constant. On the other hand, we can see that for very short scaterring times τ the characteristic is almost constant and for longer τ the decrease shifts to the lower frequencies. On the contrary, the imaginary part of the conductivity, which is describing the absorption, has a global maximum in the area of the largest decrease of the real part, and it grows monotonically to this frequency.

1.3.2 Ballistic transport

First mentioned diffusive transport is perfectly usable for description of enough big systems, where electrons experience many collisions over the system dimensions. However on nanometer scales (the thicknesses of the layers in spintronic emitters), it should be advisable to introduce another aproach. The model of ballistic transport of spin polarized electrons by Zhu and Schneider *et al.* [17].

In this model, electrons are described by their distribution function. Thanks to the statistical physics we know that the possible states for electrons are occupied according to Fermi-Dirac distribution [26].

$$f_{FD}(E) = \frac{1}{e^{\frac{E-E_f}{k_B T}} + 1}, \tag{1.9}$$

where E_f is Fermi energy, k_B is Boltzman konstant, E energy and T the temperature. This distribution is in the limit of zero temperature the Heaviside function with the jump at Fermi energy and even in higher teperatures the Fermi energy approximately divides the occupied and unoccupied states. That means that mainly the electrons with energies near the Fermi level are taking part in transport since in order to be accelerated they have to occupy empty states at slightly higher energy. That is also the reason for defining the Fermi velocity v_f which corresponds to electrons with kinetic energy on Fermi level [26]:

$$v_f = \frac{P_f}{m_0} = \sqrt{\frac{2E_f}{m_0}}, \tag{1.10}$$

where P_f is Fermi momentum and m_0 is the electron mass.

If we consider the ultrafast optical excitation of a metal bilayer, we can describe the spin transport by the Bolzmann equation using the perturbated Fermi-Dirac distribution before and after excitation. The model from Zhu and Schneider *et al.* [17] showed that if we consider a sufficiently short stimulus (shorter than τ from Drude model) or a sufficiently short system size (limited by the mean free path), spin transport is more of a wave propagation character. The front of this wave moves at a speed of $v_f/\sqrt{3}$, so we call it ballistic. For lengths greater than the mean free path, the spin will propagate at a significantly lower diffusion rate.

Now having this formalism, we could explain what is ment by the ballistic transport and how it differs from the diffusive transport. Usual diffusive transport is based on the motion of electrons repeatedly scattered and accelerated in the direction of the external field. Ballisticly transported electrons (on small scales in nanostructures) are, on the other hand, electrons which traverse through the structure with no scaterring.

1.3.3 Relaxations of spin currents

Spin currents are said to be non-dissipative - meaning that unlike charge currents in which carriers are dispersed in a material, spin polarization can propagate through a medium without particle transfer, so there is no equivalent of Joule heating, but it certainly does not mean that spin polarization is not lost. The spin polarization (the average spin projection of the ensemble) decreases exponentially with time and thus also the distance traveled by the spin current according to the relation (1.3) The distance traveled by the spin current is in principle a well measurable quantity which we want to measure.

For this purpose, for the diffusion type of transport, the diffusion length L_s is defined as [13]:

$$L_s = \sqrt{D_s \tau_s}, \tag{1.11}$$

where D_s is spin diffusive coefficient and τ_s is spin relaxation time from (1.3). L_s ranges usually from tens to hundreds of nm in metals and more than 1 µm in semiconductors [14, 24, 21].

For balistic transport, as defined above, the spin propagation length λ_s is defined [17]:

$$\lambda_s = c\tau_s, \tag{1.12}$$

where c is directly the propagation velocity.

For more general case, where the character of the transport is unknown, it is common to use the general spin relaxation lenght λ_{rel}. Anyway with the distance l, the spin current is relaxing as:

$$\boldsymbol{j_s} = \boldsymbol{j_{s0}} e^{-l/\lambda_{\mathrm{rel}}}, \tag{1.13}$$

where j_{s0} is the inital spin current at position $l = 0$.

Lets now focus on the microscopic models describing spin current relaxation - Dyakonov-Perel and Eliot-Yafet [25, 21, 24].

Eliot-Yafet model (dominant in metals) describes the loss of spin polarization by the random change of spin projection during scaterring of the particle carrying this spin. As in spin-polarized materials, it is more probably that the scattered particle has the dominant projection of spin before the scattering event, approximately every 10^{th} to 100^{th} scattering event leads to a change in spin in metals, thus spin polarization is disappearing. This process is dominant in metals which have normally much more impurities and defects than semiconductors and the scattering is then more often.

The Dyakonov-Perel model describes the loss of spin polarization by the fact that we could look on a spin as on a magnetic moment moving in the lattice. Each particle feels slightly different external electromagnetic field depending on exact trajectory in the lattice due to the spin-orbit interaction. These fields cause precession of spin momentum and again relaxation of the spin current. After each scaterring the direction of electron movement is changed and the precesions are averaged to zero. This mechanism is thus reduced by scaterring. That is the reason why this effect is negligible in materials with small mobility (i.e., metals).

1.4 Anisotropic magnetoresistence

We will now move from out-of-plane currents in STE, the nature of which we want to study, to in-plane currents which are in the frequency range 0.1 to 2 THz (achievable in the Prague Laboratory), definitely diffusive [18]. If the studied material is FM, then this transport shows magnetoresistance.

Magnetoresistance is an extremely wide range of phenomena where the electrical resistance of a material depends on a magnetic field or, generally speaking, magnetization or any other magnetic moment such as spin accumulation. Basicaly, there are two categories of this effects. First ones are those, where the resistance is directly proportional to the external magnetic field affecting the moving charge carriers by the Lorentz force. Here we could mention geometrical magnetoresistence [26] or effects connected to higher localization of charge carriers in magnetic fields as for example Shubnikov-de Haas oscilations [37]. Second ones are the effects manifesting in magnetically ordered materials where the magnetoresistance is proportional to their inner projection of magnetization in some significant direction (current direction, crystallographic orientation, magnetization of another layer ...). Very important efffects in this category are the giant magnetoresistance (GMR) or tuneling magnetoresistance (TMR) [38]. These effects observed on specially prepared nanostructures can reach the change of resistance in order of magnitude and it already has its aplications in reading heads of hard drive discs [6] or in magnetic random access memories [7]. Another extremely important effect is the anisotropic magnetoresistance (AMR).

AMR can be defined as a general change in resistance depending on the orientation of the magnetization with respect to some of the other quantities such as direction of current or crystallographical orientation, depending on the type of AMR discussed in next section. Generally we can define the AMR contrast as:

$$\text{AMR (\%)} = \frac{\rho_{||} - \rho_{\perp}}{\rho_{\perp}} \cdot 100\%, \tag{1.14}$$

where $\rho_{||}$ and $\rho_{\perp}$ are resistances measured for case of magnetization perpendicullar and parallel to the direction of current. Typical size of this effect is 1 to 10 % [39]. AMR is very useful, although it is a smaller effect than GMR, because it allows measurements on antiferromagnets (unlike GMR) as it is mostly even in magnetization. That makes this effect highly interesting for potential further applications in antiferromagnetic spintronics. At the same time, it has recently been demonstrated that the THz analog of electrical AMR is also observable [18, 40]. That is the reason, why we want to focus on this phenomenon.

1.4.1 Origins and symmetries of AMR

The AMR has in general, as it is phenomenon of more than one physical origin, quite complicated structure. With neglecting the higher terms, we can describe its symetries by the phenomenologic equation [41]:

$$\frac{\rho - \rho_{\text{avg}}}{\rho_{\text{avg}}} = C_1 \cos(2\alpha) - C_{1,c} \cos(4\theta - 2\alpha) + C_2 \sin(2\theta) - C_4 \cos(4\theta), \qquad (1.15)$$

where ρ is the resistance measured for given angles α and θ, defined in Fig. 1.4, and ρ_{avg} is the averaged longitudinal resistance. $C_1, C_{1,c}, C_2$ and C_4 are constants indicating the strength of the types of AMR typical for given material.

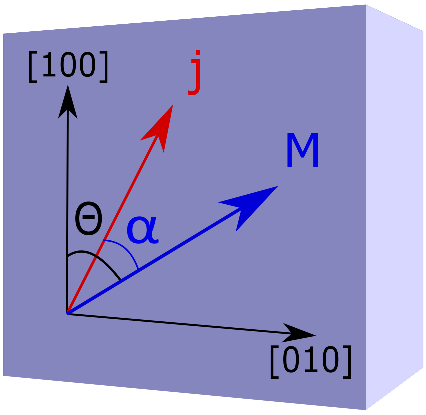

Figure 1.4: Defining figure of angles for AMR symmetries. Black arrows show the crystallographic axes, blue arrow shows direction of magnetization M, red arrow shows the direction of current j (or polarization of THz pulse).

The first term in eq. (1.15) represents the classical noncrystaline AMR where only the angle α in between magnetization and the direction of current plays role. Usually, this is the biggest AMR contribution [41]. It originates in the previously mentioned spin-orbit coupling, the bridge between magnetic moments and electron motion, which makes scatterings of electrons dependent on the magnetization of the sample [39]. This effect is nicely observable both in polycrystalline and single crystalline materials.

The third and fourth term in eq. (1.15) represent the crystalline contribution of AMR. It is the AMR measureble only in materials with single crystaline structure and it dependes only on the angle θ between the magnetization and crystal orientation as in Fig. 1.4. Two terms suggest that symetry of this effect can be uniaxial or cubic, dependeing on the symetries of crystal lattice or strain. This effect is completely independent on the direction of current because it originates in changes of the band structure for different orientations between crystal lattice and magnetization. Changes in the band structure lead to changes of DOS at Fermi surface, so they affect the mobility and, thus, the overall conductivity [41, 42, 43].

Finally, the second term describes the "mixed" cross-crystaline AMR. It is the AMR depending on both α and θ angles. It is higher order in the expansion in angles and it is like a classic noncrystalline AMR, but different in each direction to the crystal. This is what Zeng *et al*. refers in cobalt-iron (CoFe) [19].

1.4.2 THz investigation of AMR

THz radiation, as already mentioned, shares some properties from optics and some from electronics. As it has low photon energies, it does not induce any interband transitions of electrons and the conductivity measured using THz radiation transmittance is quite similar to the clasical electrical conductivity (the THz conductivity measurements are described in Method section). From THz measurement we reach the Drude-like spectral dependence of conductivities which can be then easilly extrapolated to the zero frequency, so the DC conductivity is obtained.

Having this idea, we can realize THz measurement of AMR. The thin magnetized sample is put in the path of THz radiation and the transmitted field is evaluated. The direction of THz linear polarization plays the role of the current direction in Fig. 1.4 and other parameters remain the same.

This type of THz AMR measurement was recently published by Nádvorník *et al.* [18] in NiFe, Co and Ni samples. As the nature of noncrystalline AMR was believed to comes from scaterring events only, the spectral dependence of this phenomenon should copy the conductivity (Drude-like) and have same relevant parameter: τ. However, using the THz detection method spanning over large frequency range, they show that there is a possibility to distinguish scattering-dependent and independent parts of noncrystalline AMR by analyzing the non-Drude-like components in measured spectra.

In this thesis, on the other hand, we want to focus mainly on the first THz measurement of the crystalline AMR. For this purpose, we will work with CoFe samples on which the huge crystalline part of AMR was already demonstrated in DC electrical measurements by Zeng *et al.* [19].

1.4.3 AMR in cobalt-iron

CoFe is a ferromagnetic material exceptional for its AMR which looks to be fully crystalline, coming only from its band structure. It reaches (in AMR "easy axis" - the direction in which AMR is the biggest) around 2.4 % and was measured and theoretically described by Zeng *et al.* [19].

Measurements from this article were done fully electrically as it is usual. To have a chance to probe the AMR under different orientations of crystal latice, quite complex sample with an extensive use of litography has to be fabricated. The scheme of the sample is shown in Fig. 1.5 (a). The blue bar is 10 nm thick $\mathrm{Co}_x\mathrm{Fe}_{1-x}$ fabricated to the shape of half-circle in order to have a possibility to measure the longitudinal resistance ρ_{xx} and transversal resistance ρ_{xy} using the gold contacts around the whole half-circle with continuously varying angle θ between [110] orientation of the lattice and the direction of the current (we define θ in previous section differently, between [100] orientation of sample and the direction of magnetization).

In Fig. 1.5 (b), (c) we could see the variation of ρ_{xx} and ρ_{xy} for one particular composition of Co and Fe under two different oriantations of the lattice under the whole 360° rotation of magnetization drived by enough strong external magnetic field, described with angle α as it is shown on 1.5 (a).

Finally in Fig. 1.5 (d) there is the value of AMR contrast defined in (1.14) for the whole 180° range of orientations of the lattice and for several compositions x

in $\mathrm{Co}_x\mathrm{Fe}_{1-x}$.

These results show that the AMR in CoFe (best seen for the composition approximately $\mathrm{Co}_{0.5}\mathrm{Fe}_{0.5}$) is absolutely dominated by the mixed, cross term from eq. (1.15) and changes by factor of 40 only by varying the crystallographic orientation are there.

In the article [19], the theory it is described too. AMR in CoFe is explained by the anticrossing effects in the band structure sensible to the magnetization in mixed band structures of Co and Fe which were calculated *ab initio*.

As the AMR in CoFe is interesting on its own and fully electrical measurements need quite complex fabrication of samples, we have chosen as a goal of our work to measure the AMR on CoFe using THz radiation. Our approach could bring results on samples without any electrical contacts and also the spectral picture of magnetoresistance in THz spectral range.

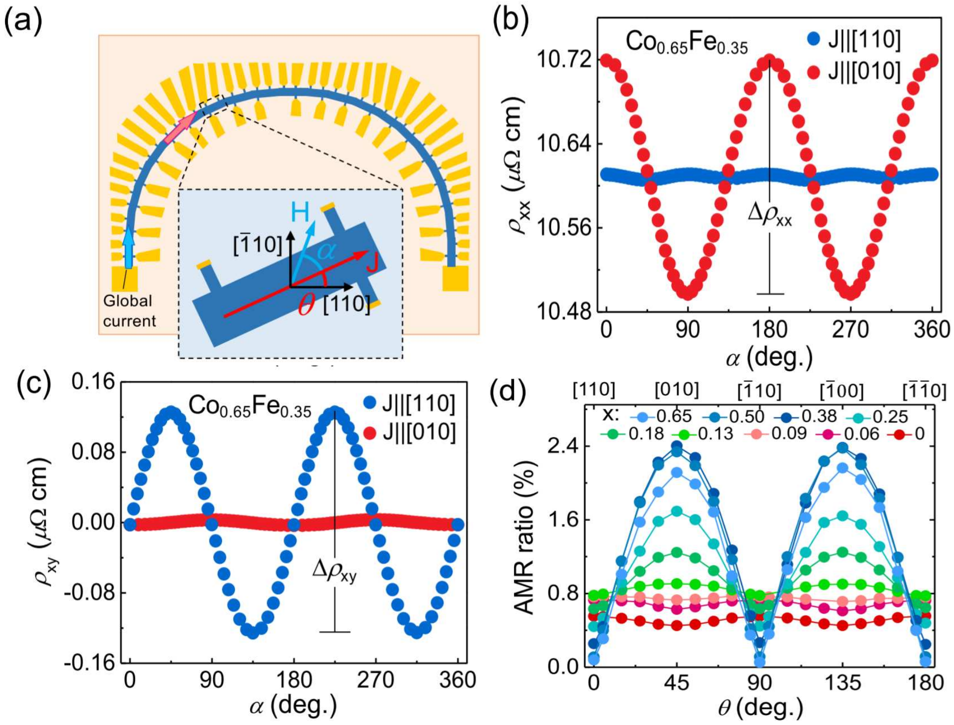

Figure 1.5: AMR measured in CoFe by Zeng *et al.* [19]. a) Scheme of the device used for measuring of the cross-crystalline AMR - blue bar made of CoFe with gold contacts and detail scheme introdusing the notation of angles. b) and c) Modulation of resistivity ρ_{xx} and ρ_{xy} versus angle α for current oriented in crystalographical orientations [100] and [110]. d) The size of AMR depending on crystalographical orientation of CoFe for several ratios of cobalt to iron. Taken from [19]

2. Methods

2.1 Experimental setups

After the theoretical introduction of the physical effects that we want to explore, we have to focus on the experiment design. The work presented in this thesis was done in two laboratories - the THz laboratory at Freie Universität, Fritz Harber Institute of Max Planck society in Berlin and the new laboratory of optospintronics and THz spectroscopy at Charles University, Faculty of Mathematics and Physics at the department of Chemical Physics and Optics in Prague.

2.1.1 Berlin and Prague setups

Firstly, I would like to go through the layout of the Berlin setup quite precisely, so that the reader could understand the principles of THz time-domain spectroscopy and then I want to focus on the differences in the Prague setup.

The basic scheme of the Berlin setup is shown in Fig. 2.1.

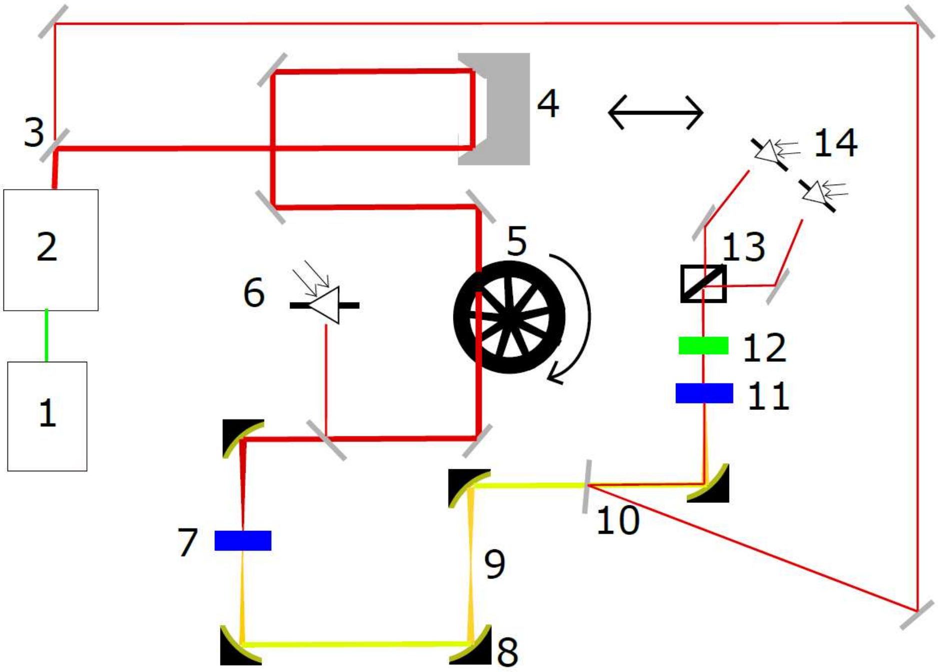

Figure 2.1: Scheme of the setup in Berlin laboratory taken from my bachelor thesis [16].

In positions (1) and (2), we create short optical pulses which, in position (3), we divide into the generation beam and the gating beam. The generation beam continues through a delay line, a chopper and a system of parabolic mirrors where THz pulses are generated. These are detected using the gating beam and the nonlinear optics in position (11) and further.

In the position (1), there is a Nd:YAG laser generatig the continuous wave laser beam at 532 nm. This beam is then guided into the cavity with Ti:Sapphire crystal (2) where, thanks to the nonlinear effects and passive mode-locking, the ultrashort 10 fs long laser pulses at central vawelenght 790 nm are generated. The spectrum of the pulses can be characterized by the Gaussian profile with full width at half maximum (FWHM) approximately 90 nm. The repetition rate is 80 MHz and the continuum output power is 600 mW. That means maximal fluency (energy per pulse) approximately 7.5 nJ.

Further in position (3), the beam is split into the gating branch (thinner line) and the generation branch. The beam in the generation branch is then passing through the delay line (4) and the beam chopper (5) which modulates the beam intensity. Precize shape of the modulation, needed further for a demodulation in phase-synchronized lock-in amplifier, is detected by photodiode at position (6). Then the beam approaches the series of five parabolic gold mirrors (8) aligned so that in position (7) and (9) we have the beam focus and between the second and third and the fourth and fifth mirror the beam is collimated. At possition (7), it is possible to generate THz pulses using spintronics emitters and at possition (9) it is possible to place a sample we want to study by THz radiation. At possition (10), there is the silicon wafer set so that the gating beam is reflected in the same path as the THz radiation. The whole part of the setup where the THz radiation is propagating (from (7) to (11)) is covered by a plastic flowbox where the dry air is pumped. So, the propagation of THz radiation is not affected by the dispersion or absorption on the water wapour. At positon (11), there is placed some noncentrosymmetric nonlinear optical crystal (ZnTe or GaP) enabling the detection of THz pulses using half-wave plate (12) and the balanced optical bridge (13) and (14).

Having an idea how the experiment is built, we could mention the differences in the Prague setup. The source of femtosecond pulses in Prague is produced by the Pharos laser system which allows us to change the repetition rate of pulses from 10 kHz to 1 MHz while keeping the same integrated intensity. This means that we can vary fluence per pulse from tens of µJ to 1 mJ. It is possible to divide the nuber of pulses in the pulse train and also to atenuate the maximal laser output 10 W up to 1.5 W. The central wavelenght of output pulses is 1030 nm - so the near IR. The duration of the pulse is approximately 130 fs. The beam is splited immediately behind the output in proportion 1 to 4. The branch used for THz experiment is the weaker one - so the maximal output for THz experiments is 2 W. That means maximal fluency (with lowest repetition rate 10 kHz) approximately 200 µJ. Except for a slightly different arrangement on the optical table, there is a difference in parabolic mirrors which are made of silver (instead of gold). Another difference is the fact that during the measurements for my thesis there still was not constructed the flowbox for dry air in the part with THz radiation, so the THz curves are affected by the dispersion and absorption on water vapour. The optical beam incoupling (in fig. 2.1 the place 10) is made instead of silicon vafer by a beamsplitting pellicle - very thin (hundreds of nm's) membrane set so that the Fabry - Perot-like reflection of the gating beam is constructive in the direction of THz beam. Examples of normalized THz curves and their spectra generated from the same spintronic emitter measured in approximately 1 minute on these two setups are shown in fig. 2.2.

It is nicely obsevable that in Prague the water vapours cause aditional oscillations in waveform after the main oscillation as the radiation is dispersed or

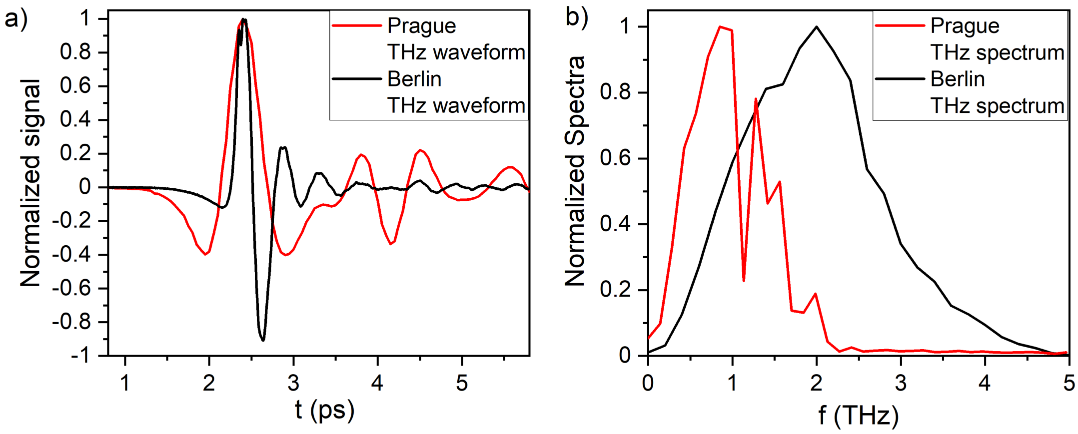

Figure 2.2: a) Normalized THz waveforms and b) their spectra emitted from spintronic emitter consisting of 2 nm CoFeB and 2 nm Pt (CoFeB(2)/Pt(2)) measured in Berlin at Fritz Harber Institut and in Prague at Department of Chemical Physics and Optics

absorbed and reemitted from the water molecules. For the same reason, we see the gap in THz spectra among 1.2 THz. However, different crystals for detection were used in both setups (Prague - 2 mm thick GaP, Berlin - 1 mm thick ZnTe). It is possible to see that the Berlin setup is able to detect up to 5 THz (and with thinner detection crystals even to higher frequencies), but in Prague setup the detection is optimized only up to 2 THz and additional measurements have shown us that the spectral range will not be wider with thinner detection crystal. It can be caused by significantly longer excitation pulses and different geometry in Prague setup.

Despite the fact that the Berlin setup has its undoubtedly advantages in wider specta and constructed flowbox for dry air, we have to take into consideration that Prague setup is quite young, still developing setup, the dry air flowbox is beeing constructed nowadays and there are the plans to construct noncolinear optical parametric amplifier so we will be able to produce shorter pulses on variable wavelenghts and then probably measure THz pulses with wider spectra. Big advantage in case of Prague setup is also the variability of Pharos laser system itself, possibility of producing much stronger pulses and the stability of them.

2.1.2 Detection and evaluation of THz pulses

As THz time-domain spectroscopy is a quite special method enabling to reconstruct directly the whole THz waveform including its phase, it is natural that the detection of this radiation is more complicated than in ordinary optical measurements, as the absorption semiconductor-based detectors are sensitive only to the intensity of the incident radiation. In the previous pragraph, there were some hints speaking about nonlinear optical crystals and the balanced optical bridge, but now lets go through it more in detail.

The detection is based on the second order nonlinear optical phenomenon - Pockels effect. The electric polarization in a nonlinear optical crystal is possible to express using the susceptibility tensor χ and expanded in electric field orders like [44]:

$$P_i = P_{0i} + \sum_j \chi^{(1)}_{ij} E_j + \sum_{j,k} \chi^{(2)}_{ijk} E_j E_k + \sum_{j,k,l} \chi^{(3)}_{ijkl} E_j E_k E_l + ... \tag{2.1}$$

Now, if we have a non-centrosymetric nonlinear optical crystal, the $\chi^{(2)}$ member of susceptibility expansion is generally nonzero. The higher terms of the expansion are then negligible. Further, if we assume in (2.1) zero initial polarization P_{0i}, we consider E_j to be an optical field E_{opt} and E_k to be an external elctrical field E_{ext}, we could write (for simpicity without indices assuming the mutual orientation of fields and crystal so that the $\chi^{(2)}$ member is nonzero) the final equation [44, 45]:

$$P = \chi^{(1)} E_{opt} + \chi^{(2)} E_{opt} E_{ext} \tag{2.2}$$

The fact that the polarization of optical radiation is directly proportional to the external electric field, as we see. in (2.2) is called the Pockels effect.

Understanding the Pockels effect, we could start with explaining THz radiation detection - the electro-optical sampling (EOS). Scheme of EOS, taken from, [46] is shown in Fig. 2.3. Firstly, on the left side of the figure, there is an incident gating short optical pulse polarized perpedicularly to the THz pulse. These two incident fields approach the nonlinear optical crystal where, due to the Pockels effect (the role of E_{ext} plays the THz field), the linear polarization of gating beam is changed to eliptical polarization with high excentricity. Then this radiation goes through quater-wave plate which changes its polarization to almost circular. Next element is Wollaston prism which splits the vertical and horizontal part of the polarization to two paths which are detected by two balanced photodiodes. The whole process leads to the direct scaling of difference signal with diodes on the size of THz field. By delaying the gating and THz pulses, it is thus possible to reconstruct the entire THz electric field waveform.

The chosen nonlinear optical crystal is for the detection crucial. The elements of $\chi^{(2)}$ are different for different materials and the wavelenghts of the gating beam. Moreover, the refractive index for THz field is different from that for the optical (or near IR) field - that means that only lower frequencies are phase-mached (they are propagating together) in the crystal. The thicker the crystal is, the stronger is the low pass filter for THz frequencies. On the other hand, the thinner crystal, the weaker signal. Also the time duration of gating beam defines the temporal sensitivity of the detection - the longer pulse, the bigger area of THz waveform is probed and it plays the role of averaging and rounding the curve - again a low pass filter [9, 10].

As the process of EOS has some similarities with classical pump-probe experiments, it is not a surprise that the highest noise affecting the measurement is the $1/f$ noise. It is called $1/f$ for its spectral dependence which is indirectly proportional to the frequency and it is considered to be originated in electric contacts in electronics. That is the reason for using phase-sensitive Lock-in amplifiers [9]. The priciple of their operation is that we modulate the signal with a periodical function before detection - in our case mechanically by the chopper (position 5 in fig. 2.1). It causes shift of the signal in spectral domain to the frequency of the chopper. Then in Lock-in, we demodulate the signal which is spoiled after

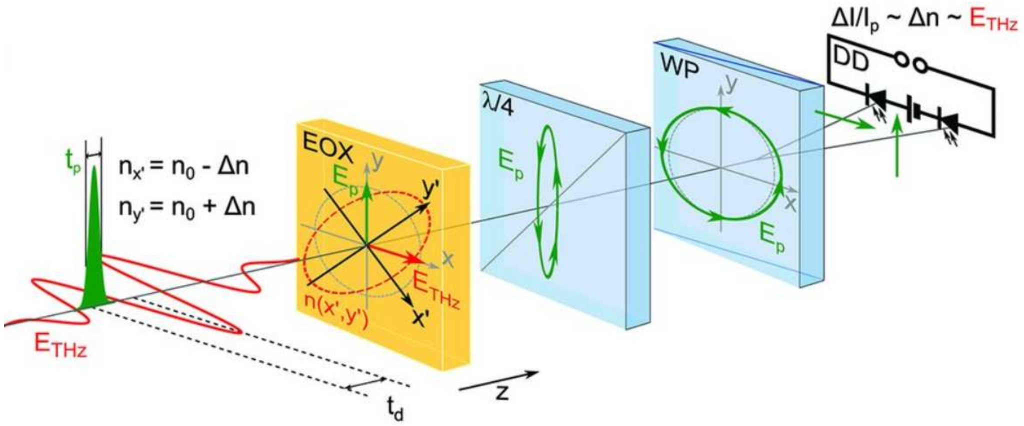

Figure 2.3: Scheme of operation of the electro-optical sampling. The THz pulse hits the nonlinear crystal together with one order of magnitude shorter optical pulse. The linear polarizations of the pulses are perpendicular to each other. The originally linear polarization of the optical pulse changes to an elliptical one due to the Pockels effect, the eccentricity of which is significantly reduced by the passage through the quarter-wave plate. The resulting almost circularly polarized pulse is divided by a Wollaston prism into two perpendicular linearly polarized components, which are detected by photodiodes. The difference signal from the diodes corresponds to the THz field and the entire THz pulse is reconstructed by the delay of the optical sampling pulse. Taken from [46]

the detection by the $1/f$ noise. As the noise was not modulated, we could get the original signal without the aditional noise of the detectors.

2.2 Conductivity measured by THz radiation

One of the areas where time-resolved THz spectroscopy achieves amazing results is the direct measurement of complex optical quantities such as refractive index or conductivity of thin films [11].

The basic idea is that any field passing through the sample is affected so that in the time domain the resulting transmitted field is a convolution of the original field and the response function of the layer. Since, in the experiment, we can measure not only the intensity but also the phase of THz electric fields, there is the possibility to infer the spectral information of the transmitted field. Than, thanks to the powerful Fourier transform, we obtain the product in the frequency domain instead of the convolution in time domain. Therefore, from the ratio of the field measured after passing through the sample and the field that passes through the setup in which the sample is not placed, it is possible to obtain very good information on material response free from all other instrumental functions of the experiment.

We will now analyze the specific case of the conductivity measurement of a thin (with respect to THz wavelength and absorption) metal layer deposited on an optically inactive substrate. Ssamples can be divided in two half-spaces composed of substrate with refractive index n_1 and air with refractive index n_2, between which there is a very thin conductive metal layer whose conductance is σ and thickness is d. In the approximation for the thin metal layer, we then obtain for the ratio of the field passed through the sample $E(\omega)$ and the field passed only through the substrate $E_{\mathrm{ref}}(\omega)$ the Tinkham formula [47].

$$\frac{E(\omega)}{E_{\mathrm{ref}}(\omega)e^{i\Delta\phi}} = \frac{n_1 + n_2}{e^{i\Delta\phi}(n_1 + n_2 + Z_0 G(\omega)),} \tag{2.3}$$

where $Z_o = \frac{1}{\epsilon_0 c} \approx 376.74\Omega$ is the impedance of vacuum, $G(\omega) = \int_0^d \sigma(\omega, z)$ is the conductance of the whole sample and the term $e^{i\Delta\phi}$ refers to the fact that due to the non-perfect flatness of the substrate, there could be some phase change between the referencial field and the field passing through the sample. $\Delta\phi$ is than equal to $\frac{(n_2-n_1)\omega\Delta d}{c}$, where c is the vacuum speed of light and Δd is the difference in substrate thickness. In a real experiment, the uncertainty in phase change is compensated by averaging of multiple measurements at several places on the sample and by additional fitting of the parameter $\Delta\phi$ (directly tied to the uncertainty of the thickness of substrate Δd) so that the final conductivity maximally fits the Drude model (1.8) described in previous section.

Then it remins only to express the conductivity $G(\omega)$ from the equation 2.3.

2.3 Parameters of STE affecting THz emission

In the theory chapter, we have defined spin currents and mechanisms of their relaxation. Considering the situation that we want to reconstruct spin polarization life time or spin relaxation lenght using spintronic-based THz emmision, it is essential to understand all factors affecting the amplitude of emitted THz radiation.

Firstly, we have to focus on THz conductivity and the overall thickness of the sample. Impedance of the sample is possible to express as [12]:

$$Z(\omega) = \frac{Z_0}{n_1 + n_2 + Z_0 \int_0^d \sigma(\omega, z)dz} = \frac{Z_0}{n_1 + n_2} \frac{E(\omega)}{E_{\mathrm{ref}}(\omega)e^{i\Delta\phi}} \tag{2.4}$$

Then, using generalized Ohm's law, we could express the THz field as:

$$E(\omega) = eZ(\omega) \int_{d_{\mathrm{FM}}}^{d} j_c(\omega, z)dz, \tag{2.5}$$

where d_{FM} is the thickness of ferromagnetic layer. The charge current could be expressed via ISHE by the spin current and spin Hall angle as $j_c = \gamma j_s$. The integration comes through the whole thickness of the nonmagnetic part of the sample using the coordinate system shown on fig. (1.2).

To get the final spin current j_s in nonmagnetic part, we have to consider back reflections like in the Fabry-Perot interferometer and sum up all the contributions (as shown in my Bachelor's thesis [16]). Then we obtain:

$$j_s(z) = j_s(d_{\mathrm{FM}}) \frac{\sinh[(d - z)/\lambda_{\mathrm{rel}}]}{\sinh(d_{\mathrm{NM}}/\lambda_{\mathrm{rel}})}, \tag{2.6}$$

where λ_{rel} is the relaxation lenght of spin current in NM from (1.13).

At the end, we consider that the magnitude of the input spin current $j_s(d_{\mathrm{FM}})$ depends on the excitation in magnetic part of the sample, which is proportional to the density of absorbed energy A/d and the ability of spin current to transfer the interface t_s. Then, after integration of the equation (2.6), we get the final THz field as [12]:

$$E(\omega) \propto \gamma t_s \lambda_{\mathrm{rel}} \frac{A}{d} \tanh(d_{\mathrm{NM}}/2\lambda_{\mathrm{rel}}) \frac{1}{G(\omega)}, \tag{2.7}$$

where we used the relation between conductivity and impedance $G = \frac{1}{Z}$

2.4 THz measurement of AMR

Second goal of this thesis is to demonstrate the measurement of AMR on CoFe using THz transmission spectroscopy. The basic idea, how to measure the AMR using THz spectroscopy as well as the previous fully electrical measurements of AMR on CoFe, were both already described in the theoretical part. Now, we will describe the concrete experimental realization.

By placing a thin sample deposited on a transparent substrate in the focus of THz radiation (position (9) in Fig. 2.1) and applying here strong enough and homogenious magnetic field, we could measure the transmitted THz field in case of parallel magnetization and THz linear polarization $E_{\|}$ and the transmitted field in case of perpendicular THz polarization and magnetization $E_{\perp}$. Using the equation (2.3), fact that we measure on one place, so the phase shift $\Delta\phi$ is the same, and definiton of resistance as the inverse value of conductance $\rho = d/G$ we could express:

$$\frac{E_{\perp} - E_{\|}}{E_{\|}} = \frac{Z_0(G_{\|} - G_{\perp})}{n_1 + n_2 + Z_0 G_{\perp}} = \frac{Z_0 d \frac{\rho_{\perp} - \rho_{\|}}{\rho_{\perp}\rho_{\|}}}{n_1 + n_2 + Z_0 \frac{d}{\rho_{\perp}}} = \frac{(\rho_{\perp} - \rho_{\|}) Z_0 d}{\rho_{\|}(\rho_{\perp}(n_1 + n_2) + Z_0 d)} \tag{2.8}$$

In the last expression in equation (2.8), we can recognize the term defining AMR contrast in (1.14). So, the amplitude of AMR can be directly expressed from measured transmitted THz fields as:

$$\mathrm{AMR}(\%) = \frac{E_{\perp} - E_{\|}}{E_{\|}} \cdot \frac{\rho_{\perp}(n_1 + n_2) + Z_0 d}{Z_0 d} \cdot 100\% = \frac{E_{\perp} - E_{\|}}{E_{\|}} \cdot \gamma \cdot 100\%, \tag{2.9}$$

where we defined the γ factor as

$$\gamma = \frac{\rho_{\perp}(n_1 + n_2) + Z_0 d}{Z_0 d} = 1 + \frac{n_1 + n_2}{Z_0 G} \tag{2.10}$$

Using the fact, that $\rho_{\perp} \approx \rho = \frac{d}{G}$.

So, in principle, we are able to directly measure the AMR of any transparent thin sample in any crystallographycal orientation (defined only by the angle between the sample orientation and THz polarization) only by measurement of transmitted THz fields $E_{\|}$ and $E_{\perp}$ if we know the γ factor. And γ factor is changing only with refractive index, which is tabulated, and conductivity, which can be measured with THz radiation, as explaned in Sec. 2.2.

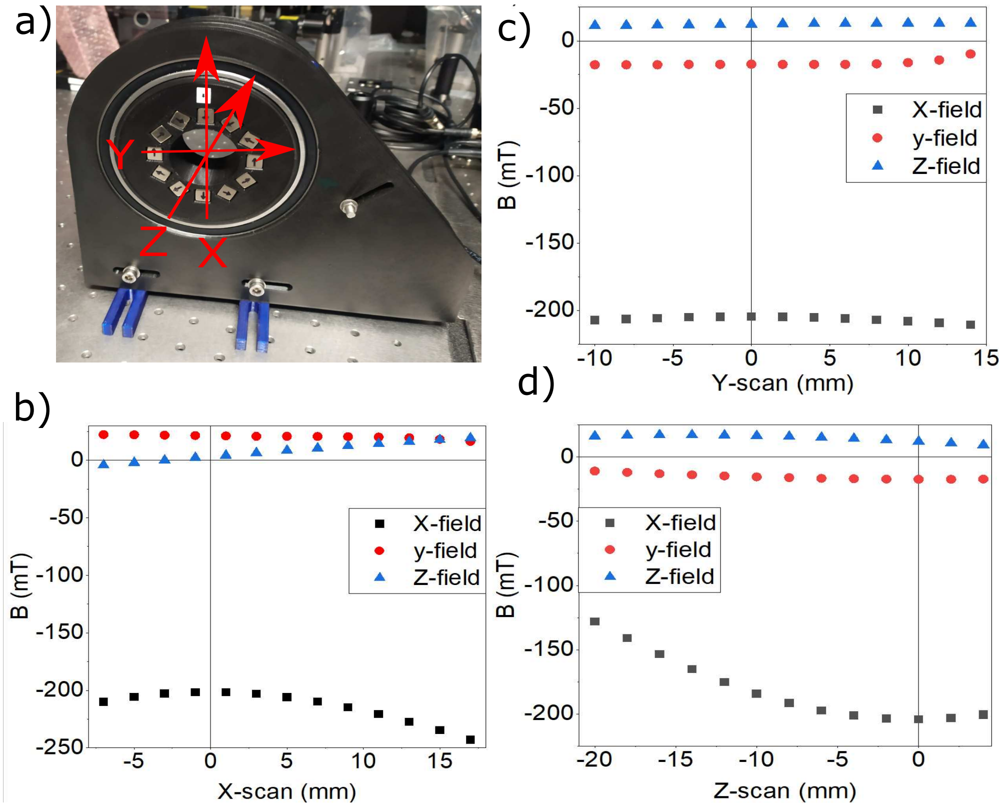

Figure 2.4: a) - Photo of Halbach rotator with coordinate axes, b), c), d) - magnetic fields measured with 3 dimensional Hall probe moving on axes with origin in the center of Halbach cylinder

Let us now find out how we can realize a homogeneous, sufficiently strong and easy to manipulate magnetic field around the sample. In our case, we used permanent neodym magnets with magnetic field above 200 mT on their surface placed into a plastic rotator made by a 3D printer in the arrangement of the Halbach cylinder [48]. The photo of our Halbach rotator is shown in Fig. 2.4 a). This rotator was constructed thanks to the work of our collegues Dr. Kevin Geinsdorf and Andrej Farkaš. The magnetic field measured on axes x, y and z with origin in the center of the Halbach cylinder was measured with 3-dimensional Hall probe and is shown in Fig. 2.4 b), c) and d). It is nicely observable that the field reaches approximately 200 mT and it is nicely homogenious on milimeter length scales. In x and y direction, the sample will be placed precisely in the center (definitely with precision under milimeter scale) and in z direction we estimate the placement of the sasmple no further than 5 mm from the center (in Fig. 2.4 d) on position 0, marked by the line) where the changes of field are no more than 2.5 %. 200 mT is, according to Fig. 3 in [19] and private communication with authors of that article, enough strong field to fully magnetize CoFe sample in in-plane direction.

2.5 Samples

In this section, we describe the design of samples enabling us to study out-of-plane spin-polarized electron transport using THz emission as well as the methods used for fabrication of all studied samples in this thesis.

2.5.1 Design of samples for THz emission experiment

As we already introduced the mechanism of THz pulses generation from spintronic emitters, we know that the process includes the transport of spin-polarized electrons from magnetic layer to nonmagnetic layer with big spin-orbit coupling. There, due to the ISHE, the conversion of spin current into the perpedicular charge current is involved and THz radiation is emitted. Our idea is to place another metal layer working as a spacer in between the feromagnetic and the nonmagnetic layer with spin-orbit interaction. This additional spacer is need to be traversed by the spin polarized electrons during the proces of generation of THz pulses. By varying the thickness of this layer, we could study the spin relaxation length in copper by analyzing the changing THz emission. The amplitude of the THz emission with taking into account the changing conductivity (measurable also from THz transmition as described before), thickness and absorbance of the sample (affecting the THz emision according the equation (2.7)), can give us the information about the spin relaxation length. Moreover, by observing the time shifts of THz waveforms emitted from samples with different thicknesses of metal spacers, we could reconstruct the time of flight of the spin polarized electrons through the spacer, so the exact speed of these electrons.

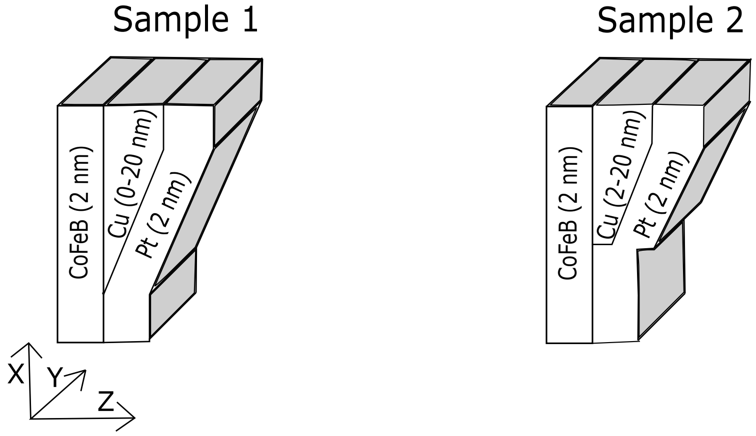

Figure 2.5: Schematic picture of samples used for measurement of speed of spin polarized electron transport. Both samples consist of 2 nm CoFeB layer, copper wedge with constant gradient (in sample 1 starting from 0, in sample 2 starting by 2 nm leaf) and 2 nm thick Pt layer, deposited on sapphire substrate in both cases.

For this purpose we have produced samples schematically pictured in Fig. 2.5. Instead of many samples with differently thick spacers we have two of them that were fabricated so that the spacer makes a wedge with constant gradient. So, by changing the place on the sample where the THz emission is realized, we can vary the thickenss of the spacer. For the examined material we chose copper with negligible spin-orbit interaction [14]. The thicknesses and materials for ferromagnetic layer and the nonmagnetic layer with spin-orbit interaction (also shown in Fig. 2.5) were chosen based on our experiences from my bachelor thesis [16] and the article devoted to optimalization of spintronic emitters [12].

2.5.2 Fabrication of samples for THz emission experiment

The samples for THz emission experiments were fabricated at the University of Greifswald in the group of prof. Markus Muenzenberg. The used technique was electron beam evaporation [49]. It is a method where electron beam is focused on bulk material which is, together with substrate, placed in vacuum chamber. The evaporated (by heating by electron beam) material is deposited on the substrate and by controlling all the growing parameters it is possible to fabricate samples even on nanometer scale precision needed for our measurements. The wedge is made by the shutter moving during evaporation.

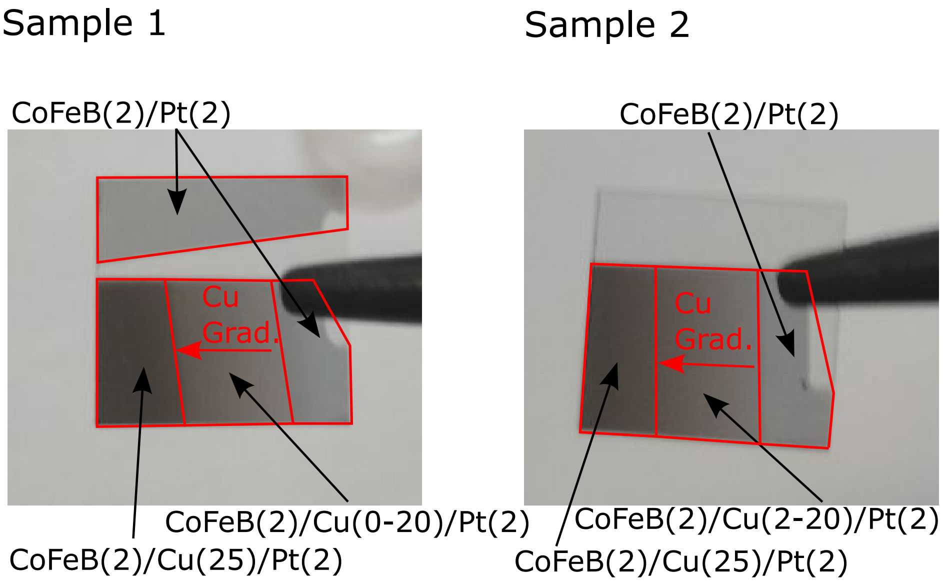

Figure 2.6: Photo of Sample 1 and 2 with labels showing areas with apropriate layers. The gradient of copper is in both cases 3.1 nm/mm (space thickness/lateral length).

The photo of previously described samples for THz emission experiments is shown in Fig. 2.6. We see that both samples have areas with bare substrate needed for measurement of reference THz waveforms during conductivity measurements. Then, there are successions of areas with only spintronic bilayer CoFeB(2)/Pt(2), with copper wedge with stable gradient 3.1 nm/mm (spacer thickness/lateral length) between the spintronic bilayer and with flat 25 nm thick copper spacer. This enable us to measure THz emission on several places with no copper spacer and then on the copper spacer, so that we may be able to distinguish the exact place of copper wedge begining. Moreover, there is an area of

CoFeB(2)/Pt(2) on sample 1 next to the wedge where we can measure the control THz waveforms during measurements of THz waveforms time shifts. This enable us to estimate shifts caused by imperfect substrate flatness.

2.5.3 Fabrication of samples for THz AMR measurement

The sample 3, consisted of cobalt-iron (CoFe), was provided by our Chinese colleague prof. Yizheng Z. Wu from Department of Physics, State Key Laboratory of Surface Physics, Fudan University, Shanghai 200433, China and it is one of the samples from series used by Zeng *et al.* [19]. There was no litography (unlike on samples used in the article [19]), only there was a part of bare substrate and of 10 nm thick $Co_{0.5}Fe_{0.5}$. 0.5 mm thick MgO in [100] orientation was used as a substrate. The fabrication method was moleculas beam epitaxy (MBE) [49], the thickness of the sample was monitored by the reflection of high energy electron diffraction (RHEED) [49].

2.6 Gaussian beams and their propagation

In most optical experiments (including ours) working with laser beams, the behaving and propagation of the beams is nicely described by Gaussian optics. Part of our experiments will be focused on evaluating the phase shifts of THz waveforms induced by the propagation through a copper spacer. These shifts are estimated to be really tiny, so all the factors affecting them (such as changes in beam propagation) have to be analyzed. That is the reason for introducing Gaussian optics here.

The Gaussian optical beam polarized in x axis and propagating in positive direction of z axis can be described using equation [10, 44]:

$$\boldsymbol{E}(r,z) = E_0 \boldsymbol{x} \frac{w_0}{w(z)} \exp\left(\frac{r^2}{w(z)^2}\right) \exp\left(i\left(kz + k\frac{r^2}{2R(z)} - \phi(z)\right)\right), \qquad (2.11)$$

where coordinates r and z are the radial transversal distance from the center of the beam and position on z axis, respectively, E_0 is the electric field amplitude at origin, $k = \frac{2\pi n}{\lambda}$ (λ is the wavelength, n is the complex refractive index) is the wave nuber, $w(z)$ is the radius of beam where the amplitude falls to 1/e of the value in its center, w_0 is the waist radius, $R(z)$ is the radius of the curvature of the beam wavefront and $\phi(z)$ is the Gouy phase.

For easier description of Gaussian beam properties there is the definition of Rayleigh range:

$$z_r = \frac{\pi w_0^2 n}{\lambda} \qquad (2.12)$$

Using this parameter, we can see the scheme of the Gaussian beam in Fig.2.7, where the angle θ describes the apex angle of the cone at which the radiation diverges asymptotically (in the approximation of geometric optics). As a bonus, there is the easy formula for the Gouy phase:

$$\phi(z) = \arctan\left(\frac{z}{z_r}\right). \qquad (2.13)$$

The Gouy phase is an absolut phase of the wave in the envelope which is changing from -$\pi/2$ to $\pi/2$ when the beam is going through focus.

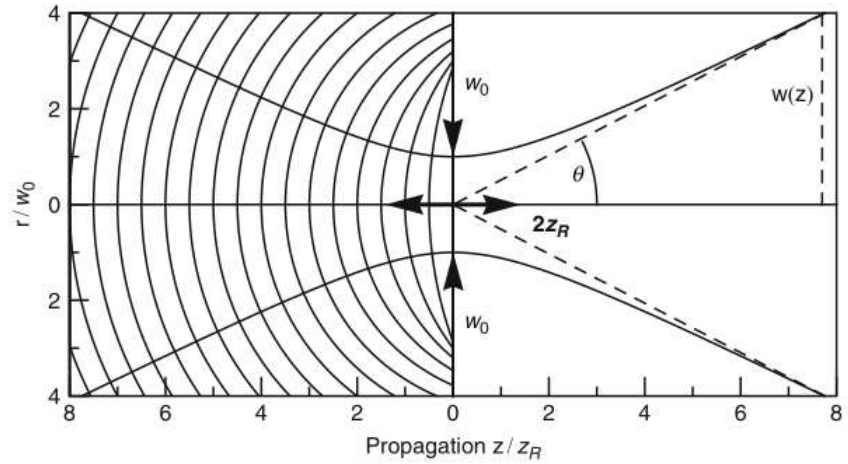

Figure 2.7: Schematical picture of Gaussian beam propagation, taken from [10]

For an effective description of propagation of Gaussian beams we will define the complex q-parameter as:

$$q = z + iz_r = \frac{1}{\frac{1}{R} - \frac{2i}{kw^2}} \tag{2.14}$$

Then, we can get all parameters describing Gaussian beam directly from the q-parameter and, at the same time, there is an easy way to calculate the change of the q-parameter after propagation of the beam through some optical device or space using the standard transfer matrices known from the matrix optics [10, 50]:

$$\begin{bmatrix} A & B \\ C & D \end{bmatrix}$$

The final q-parameter q_f is then calculated from the initial q_i as

$$q_f = \frac{Aq_i + B}{Cq_i + D}. \tag{2.15}$$

The transfer matrix is different for each case but, for example the propagation through homogenious medium of thickness d defines the parameters as A = 1, B = d, C = 0, d = 1. For lens it is A = 1, B = 0, C = $-1/f$, d = 1, where f is the focal length.

So, after this introduction of Gaussian optics, we can easily make the model of beam propagation in THz setup to reconstruct how some geometrical changes at certain point can propagate through the setup and affect the behavior further on the optical path.

3. Experiment

The experimental part of this thesis is divided into three sections. First, we want to evaluate the spin current relaxation length from the measurement of THz amplitudes and all quantities influencing THz emission (see section 2.3). Second, we want to measure the speed of this transport from shifts of THz curves which in combination with the previous result gives us the opportunity to obtain spin relaxation time and compare it with scatering time in Drude's model. In the third part we want to focus on the measurement of inplane spin currents, specifically the first THz measurement of crystalline AMR.

3.1 Out-of-plane spin current: Spin relaxation

As already was written before, we want to reconstruct the spin current relaxation length in copper λ_{rel} by evaluating of THz emission from spintronic emitters with copper spacers of varying thickness. Using the equation (2.7), we see that the emission is given by some factors which are constant everywhere on the sample - spin hall angle γ, spin relaxation length in platinum λ_{rel}, and the thickness of the platinum d_{NM}. Then, there is the ability of spins to traverse the interfaces t_s, which may be the same on the part of the sample with copper (there are two same interfaces) and same on the part without copper (one unchangin interface), but it may be different to each other. On the other hand, there are factors, which change everywhere literally on the copper wedge - the total sample thickness d, absorbed optical energy A (which is given by the absorbance a changing with thickness) and the total conductance $G(\omega)$. Thie is the reason for study of these parameters on the samples before performing the emission experiment.

3.1.1 Measurement of optical absorption

The optical absorbance was measured by a silicon power detector. Firstly, we have measured the total optical power P incident on the sample. Then we have measured the transmitted power T and the reflected power R. The absorbed power is then $A = P - T - R$ and $a = A/P$.

This measurement of absorbance was done on several places on both samples (scanning through the area with copper gradient labeled in Fig. 2.6) which were placed on a translation stage driven by a µm screw, enabling to move the sample in direction x according to Fig. 2.5).

The values of T, R and calculated A for both samples with the indicated place where we think the copper wedge started and ended are indicated by vertical lines and black arrows in Fig. 3.1. In the case of the sample 1, the total deposited power was 28.2 mW and, in the case of sample 2, it was 51 mW.

In both cases, we could see that the absorbed power at the estimated beggining of the wedge slightly increases, but then, on the rest of the wedge, the reflected power is increasing faster than the transmitted power is decreasing, so the absorbed power is also decreasing. This can happend because of the copper layer on the very beginning is so thin, that it is not enough homogeneous and in

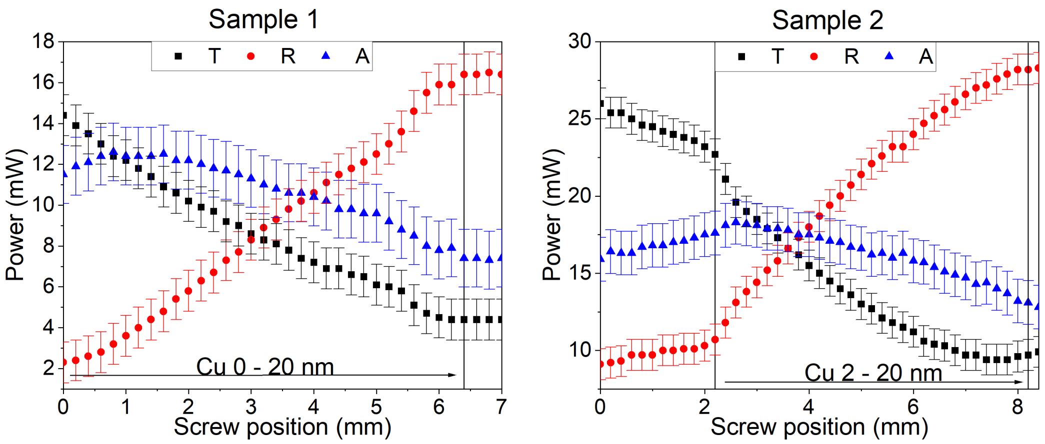

Figure 3.1: Measured transmited power T and reflected power R and calculated absorbed power A for sample 1 and sample 2

combination with the high copper diffusivity during the growth it decreases the transmittance enough but the reflectance increase is slower.

The errorbars in Fig. 3.1 are showing the estimated error ± 1 mW of the used silicon power meter. The fact that there are clearly visible changes of transmittance and reflectance on the sample 2 in front of the wedge sugggests another systematic error either in the detection scheme or in the fabrication of samples - the area before the wedge or at the begining of the wedge could be not well defined. Another observation is that on the very end of the wedge with maximal copper thicknes there may be visible another feature in the characteristics because (as shown in Fig. 2.6) there maight be a jump from 20 nm of copper to 25 nm of copper.

The dependence of the absorbance a on the thickness of copper wedge fitted by the polynomial function is shown in Fig. 3.2.

We used the third order polynomial fit $f = b_1 + b_2x + b_3x^2 + b_4x^3$. The reason for using the empirical polynomial fit without any background for it, is just to have a numerical model for absorbance, used in the further normalization of the THz emission. This allows us to have one single estimated parameter – the position of start of the wedge – in the following analysis. The parameters for both fits are in summarized table 3.1. Errors are calculated from errors of measured absorbed energy.

Sample	b_1	b_2	b_3	b_4
1	42.0 ± 0.4	1.0 ± 0.2	-0.16 ± 0.02	0.003 ± 0.001
2	35.0 ± 0.3	0.3 ± 0.1	-0.06 ± 0.01	0.0011 ± 0.0004

Table 3.1: Parameters of polynomial fit of absorbance in Fig. 3.2

The parameters have nontrivial error because of the ambiguity in exact determination of the edge of the wedge, error of the silicon intensity meter and the discused changes in front of the estimated start of the wedge. Then there is the different absorbance for the two samples (for sample 1 starting around 45 % and

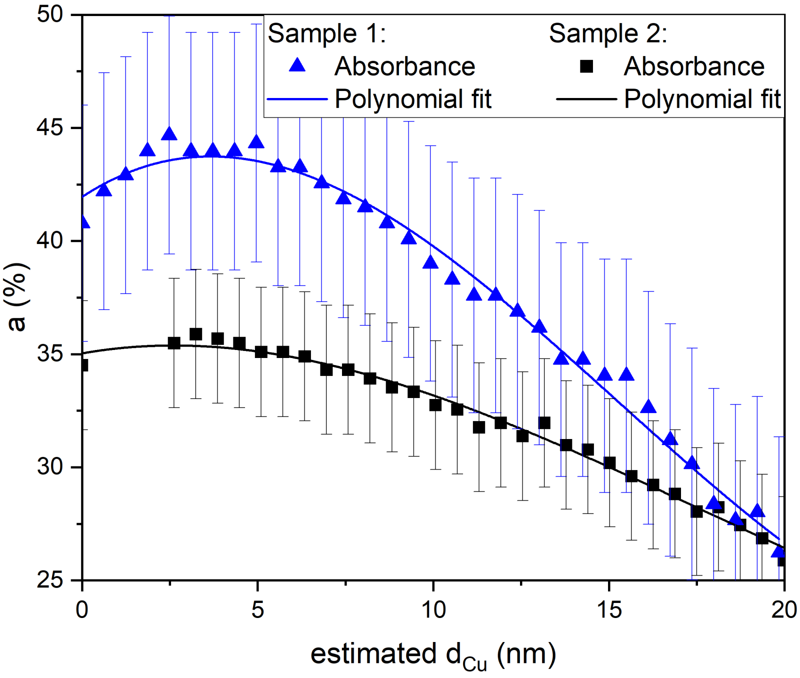

Figure 3.2: Calculated absorbance a for sample 1 and sample 2 fitted with the third order polynomial. As x axis, we have the thickness of cooper wedge estimated from 3.1

for sample 2 around 35 %), which may be partially caused by the fact that these two measuremets were done with different laser fluence, but not completely. The good message is that the absorbance is not changing significantly over the range of d_{Cu} = 0-12 nm that we plan to scan. That means that the final results of spin relaxation time will be affected maximum by variation of 8 % (when considering polynomial model versus constant mean value) which will be, as shown in following analysis, smaller than other sources of uncertainty and these results are enough good to get rid of the effect of changing THZ emission according to equation (2.7).

3.1.2 THz measurement of conductivity

Another term affecting THz emission in equation (2.7) is the conductivity of the sample. As copper is very conductive material (almost an order of magnitude greater than CoFeB or Pt [14]) and, considering samples thickness of only 4 nm (CoFeB(2)/Pt(2)) in regions without copper, the copper wedge changes the overall conductivity hugely.

The measurement of conductivity was done on sample 2 in such a way that we measure the conductivity on the place where there was no copper and then on several places with different copper thickness. The actual copper thickness was estimated based on the THz amplitude transmitted through the sample on different places. Knowing the lateral distance of measured places and gradient

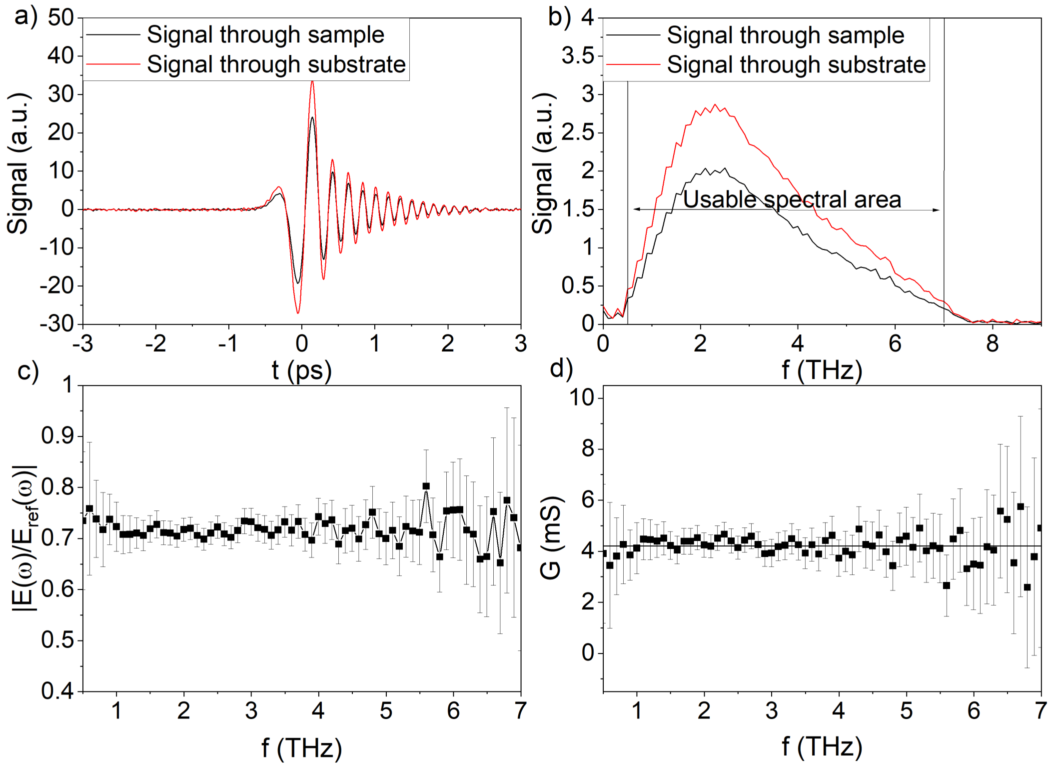

Figure 3.3: Overview on the process of evaluation of conductance of sample 2 on the place with no copper. The conductance was measured using THz waveforms emitted from spintronic emitters and detected by 250 µm thick GaP. a) Waveforms mesured through the substrate and through the sample. b) Spectra of measured waveforms with the highlighted usable spectral area. c) Ratio of these spectra with errorbars calculated from estimated white noise and d) the final conductance with indicated mean value.

of copper wedge, from the estimated start of the wegde, we can dteremine the actual copper thickness. Each measured value of conductance was evauated in such a way that we measured transmitted THz field on several places with same thickness of copper and then on several places on the nearest substrate with no deposited metal layer. This procedure helps us to minimize the phase shift $\Delta\phi$ in (2.3) caused by possible inhomogenities in substrate thickness. To reach resolution extending to higher THz frequencies, we use relatively thin 250 µm GaP as the detection crystal. For ilustration, Fig. 3.3 a) shows measured averaged THz waveforms transmitted through the sample on the place with no copper (only CoFeB(2)/Pt(2)) and through bare substrate. Having these THz waveforms and using fast fourier transform method, we can calculate the spectral composition of it. The absolute values of these spectra are shown in Fig. 3.3 b). The usable spectral range 0.5 to 7 THz is highlithed there. The ratio of these spectra needed in equation (2.3) are displayed in Fig 3.3 c). The errorbars are estimated from the assumption that our main noise is the "white niose" which is spectrally independent, affect both spectra and we estimated its value above 8 THz as 0.07(in used arbitrary units). Finaly, the real part of conductivity G (ve neglect the small imaginary part) calculated based on the equation (2.3) using known spectral dependent refractive index of used saphire substrate [10], is in Fig. 3.3 d). The errorbars are propagated from the errors in Fig. 3.3 c). The horizontal line shows us the mean, frequency independent, value which will be used to further evaluation of spin relaxation time. We used constant insted of Drude fitting because there is no obsevable spectral dependence and for further evaluation is comfortable to use just one mean value.

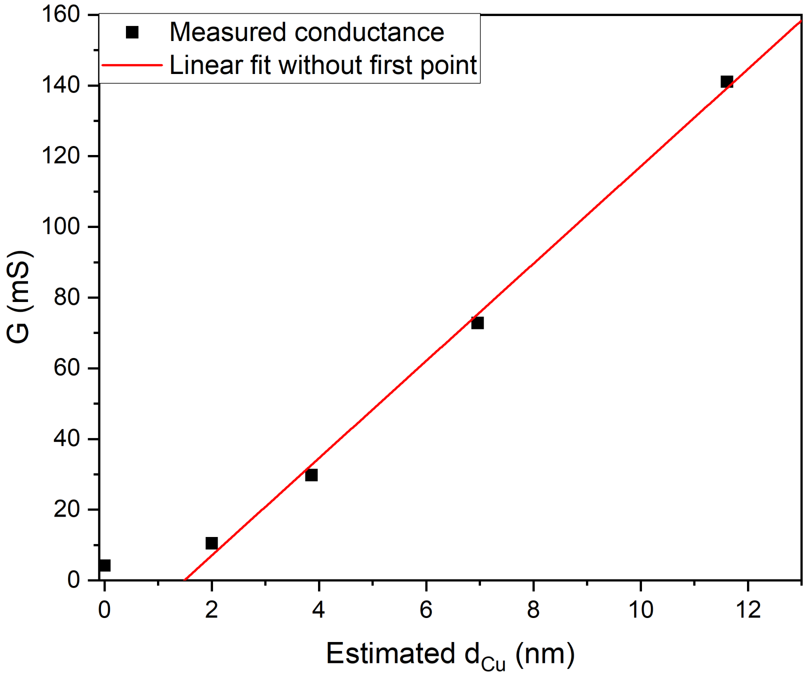

Figure 3.4: Averaged conductivities of sample 2 measured on several places with different thicknesses of copper fitted by a linear function. The errors are smaller than datapoints. Point at position d_{Cu} is the frequency-averaged value from Fig. 3.3 d).

The resulting averaged conductivities for different thicknesses of copper are shown in Fig. 3.4. The error of the averaged conductivity at one given place is smaller than the datapoint. However, the uncertainty in determination of the start of the copper wedge is much bigger. At the same time we expect linear dependence of increasing conductivity vs. increasing thickness of copper. This is the reason why we fitted only the four measured points in Fig. 3.4, which are clearly on the wedge. The points are fitted by the function $f(x) = B_1 + B_2 x$, where $B_1 = (-20 \pm 4)$ mS and $B_2 = (13.8 \pm 0.5) \cdot 10^6$ S/m, which corresponds with the possible conductivity of copper $\approx 16 \cdot 10^6$ S/m according [14] (slightly bigger value is probably given by the fact, that in [14] was used bulk material and we are using thin films). Parameter B_2 shows us quite precisely the increase of conductance per each nanometer of copper. The negative sign of parameter B_1 does not make physical sense, but this is given by the uncertainty in determining of the wedge beginning. Moreover, if we assume that the basic two layers CoFeB(2)/Pt(2) have everywhere the same conductance, we do not have to care about this absolut term. We can use $B_1 = 4.2$ mS, which is the measured conductance on the place in front of the copper wedge (first data point in Fig. 3.4). This value corresponds to the conductivity 1 MS/m which is comparable with the measurement of conductivity of sample consisting only of CoFeB(2)/Pt(2) measured in my Bachelor's thesis [16] where it was 0.75 MS/m. The difference here can be caused because of the different producers and fabrication methods of samples 1 and 2 and mentioned sample from my Bachelor's thesis. From this fitting, we can also estimate the error in determination of copper thickness as ± 1 nm. Again, we have two parameters from fitting allowing us to calculate the conductivity at various places in final measurement of THz emission as G = (4.2 + 13.8·d_{Cu}(nm)) mS using only one parameter – the final estimate of the position of copper wedge beginning.

3.1.3 Spin current relaxation length from THz amplitudes

After determination of all needed coefficients, we can focus on the actual measurement of spin current relaxation length. For this purpose, we have measured THz emission from Sample 1 and Sample 2 on different places over the wedge. Samples were placed on a translation stage driven by a µm screw, so the incident generation beam was in individual measurements pointing on places with different thickness of the copper spacer. Because these measurements were also used for evaluation of spin current speed, as described in following sections, we wanted to have the best time resolution. It means a spectral sensitivity to the maximal possible THz frequencies. This is the reason why the detection crystal was very thin: a 10 µm thin ZnTe.

The measured waveforms and their amplitudes from sample 1 are shown in Fig. 3.5 a) and b) and from the sample 2 in Fig. 3.5 c) and d). The places where we estimate starts of copper wedges are shown in 3.5 b) and d) by the vertical lines. Already now, if we compare the amplitude from sample 1 cca 0.8 mm from the place where we indicated the start, i.e. 14.5 a.u., with the second point measured on the copper wedge on sample 2 where, due to the jump, is estimated the copper thickness to be the same, giving amplitude of 25 a.u., we see that beginnings of wedges are not fabricated very precisely. There is definitely faster decrease of THz amplitude at the begining of the wedge on sample 2, but it is not an abrupt jump. The wedges have probably not well defined gradient at very small thicknesses which can happened in such growths. For further evaluation, it means that data measured near the start of the wedge will be hard or impossible to interpret and we have to bear it in mind when evaluating all the data further in this section.

To infer the final spin current relaxation length, we combine the amplitudes in Fig. 3.5 with a repeated run of the same measurements on both samples. At this point, we estimate the starts of copper wedges (marked by vertical lines) and calculate the conductivity and absorbance at each measured point using previously shown relations. After dividing the original amplitudes by the calculated absorbance and multiplying by the estimated thickness of sample and by the calculated conductance following eq. (2.7), we get final amplitudes whose exponencial decrease is given by the spin current relaxation length as described in

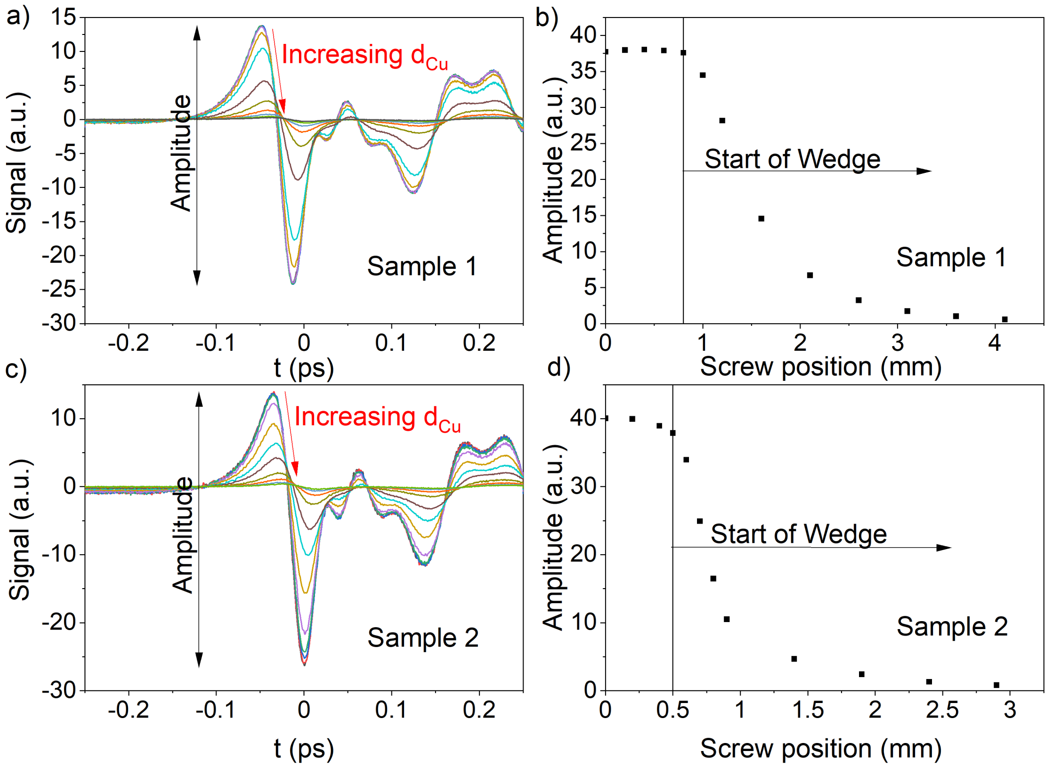

Figure 3.5: a), c) Measured THz waveforms emitted from sample 1 and 2 on places with different thicknesses of the copper spacer (range $d_{Cu} = 0$ to approx 9.5 nm). b), d) The amplitudes of measured waveforms as a function of the position of the sample with respect to the laser beam. The position where amplitudes start to decrease (the copper wedge beninning) is marked by the vertical line. Calibration of the wedge thickness: $d_{Cu} = 3.1$ nm $\cdot$ screw position from the start (mm).

equation (1.13). These results with corresponding fits are shown in Fig. 3.6.

The exact fitting function is $f = C_0 + C_1 e^{-\frac{d_{Cu}}{\lambda_{rel}}}$. We phenomenologically added an absolute term C_0 (which is not in eq. (1.13)) for better fitting ($C_0 \approx 1/6\ C_1$). As shown further, the λ_{rel} obtained from fits with constant member corresponds to our other results and previously reported value [11]. The explanation for the constant term could be the spectral dependent λ_{rel} with some low frequency part playing role also on places with thicker copper spacer (spectral filtering of THz waveforms emitted from copper wedgges is present there and described further).

The spin relaxation lengths from these fits are summarized in table 3.2. The errorbars in x direction are from the estimated ± 1 nm uncertainty of copper thicknes originating from the estimate of wedge beginning that we observed in measurement of conductance.

In Fig. 3.6 we can fully understand that the beginnings of the copper wedges are problematic. We can demonstrate it at the red datapoint on the nominally gradual wedge of sample 1. Here we see a non-monotonic trend, which is in stark contrast to the simple eq. (1.13). So this model is obviously not complete for thin spacers. The same effect is present even on black datapoints representing measurements on sample 2 - notice the black datapoint at zero copper thickness.

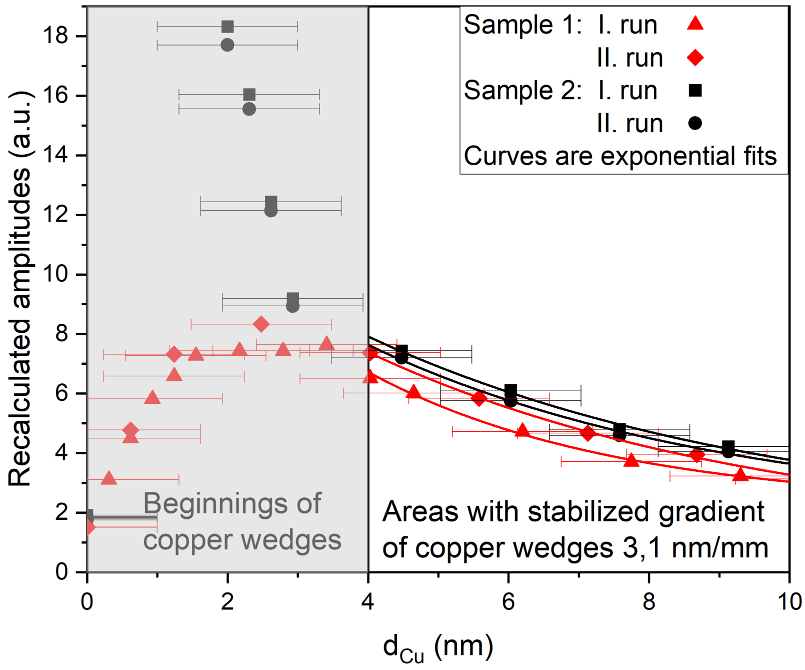

Figure 3.6: Amplitudes of THz waveforms emitted from samples 1 and 2 normalized for calculation of spin relaxation lengths. In the area of stabilized copper wedge gradient, the data are fitted by exponential function.

The considerably larger slope of the black datapoints in grey area and the bounce from the first point is definitely the effect of the wedge on the sample 2 not beginning with a clearly defined, abrupt, 2 nm jump but rather a steep gradient. Moreover, the data show that the normalized emission from the trilayer was always greater than the emissions from the bilayer.

Sample	1	1	2	2
λ_s(nm)	3.5 ± 0.8	6 ± 1	6 ± 2	5 ± 1

Table 3.2: Spin current relaxation lengths from exponential fits of data from Fig. 3.6

All these observations show us that we have to consider also the changing factor t_s in equation (2.7). t_s is the quantum transparency of the spin traversing the interface, often modeled using an additional thin layer with an enormously short λ_{rel}. The term ”spin memory loss” has been used in the literature for this [35]. Its change could explain the unmonotonous trend on the places where there is only very small amount of copper with barely defined thickness at the begining of the wedges and also the higher values of normalized amplitudes everywhere on the wedge in comparison to the place without copper. Moreover, according to the described model of spin current generation through UDM, the current is proportional to the spin voltage which is independent of DOS in NM, but dependent only of DOS in FM. Therefore, the fact that we exchange Pt for Cu should not lead to a simple reduction of j_{s0} in eq. (1.13). It's more of a change of spin memory loss t_s.

In summary, we assume that the interface CoFeB-Pt could have higher spin memory loss, than two interfaces CoFeB-Cu and Cu-Pt. Importantly the interfaces are the same in the area of stable copper gradient. The conductance G is given quite precisely in this stabilized region (we see the nice linear dependence in Fig. 3.4) and the results from both samples agree very well. As the resulting spin current relaxation length in copper we consider the mean value of fitting parameters in table 3.2. It is $\lambda_{rel} = (5 \pm 1)$ nm.

3.1.4 Robustness of results

The results of absorbance measurement, measurement of conductance and the final evaluation of spin relaxation lengths were shown in previous few sections. Each of these measurements have, however, its errors and uncertainties discused there. Let's now focus on the impacts of these uncertainties on the final result.

Firstly, there was the measurement of absorbance. Despite the expected linear dependence of absorbance on the copper thickness, we observed the nontrivial characteristic in Fig. 3.2. The changes were, on the other hand, varied only by a factor up to 11 % in the used sample area and the impact on the final result is really small. To prove this, we tried to recalculate the THz amplitudes using the averaged value of absorbance in the range from 0 to 10 nm of d_{Cu}. Fitting these data in the usable range by exponential function yields (in terms of errors) the same spin relaxation time. Comparison of originally evaluated amplitudes and those evaluated with constant absorbance is, for one of the measurements, shown in Fig. 3.7 a). So we can be sure that this parameter does not spoil the results and it is not responsible for the unexpected behavior in the grey area in Fig. 3.6.

Another parameter affecting the results is the conductivity. Here the role is much stronger than the role of changing absorbance, so there is a natural question, if the inaccurancy in determination of the start of copper wedge during the conductance measurement could not cause all the unexpected behavior and changes results. To be sure about this, we tried to calculate the final amplitudes for +/- 1 nm shift of the horizontal axis in Fig. 3.4 (i.e., reducing or increasing G as if d_{Cu} is thinner or thicker by 1 nm for all data points). These data fitted by the exponential function as before in the usable area are for the case of one of the measurements shown in Fig. 3.7 b). The spin relaxation lengths from fits are in case of higher conductance $\lambda_{rel} = 4.4 \pm 0.9$ nm, so within the estimated errors the same as the original fitted value, but for case of lower conductance, we get $\lambda_{rel} = 26 \pm 35$ nm, so five times longer and with more than 100% error. Greater than 100% error indicates that the trend is no longer fitable exponentially which is sharply against expectations. It seems that such manipulation with G leads to the unusability of the data in the whole range of measurements and therefore we do not consider it. Trying the same manipulation with conductance in other measurements brings similar results.

However, this suggest that the firstly presented $\lambda_{rel} = (5 \pm 1)$ nm is probably burdened with higher error. It also show us that by manipulation by both paramenters affecting the evaluation of THz amplitudes, we can not "repair" the data in the grey area, indicating that the behavior might be real. Indeed, all the calculated amplitudes measured on the wedges are significantly larger, than the amplitude before wedge (at $d_{Cu} = 0$), so the impact of the spin memory loss described by t_s is highly probable.

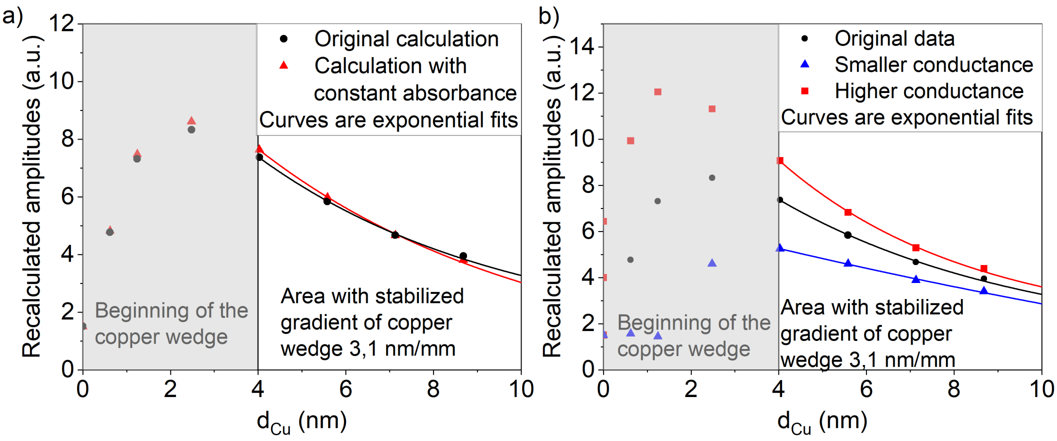

Figure 3.7: Amplitudes of THz waveforms emitted from sample 1 normalized for calculation of spin current relaxation lengths with different models of a) absorbance and b) conductance. Areas of beginnings of copper wedges are marked by grey background and the data here are not described by our exponential model. In the area of stabilized copper wedge gradient and unchanging spin memory loss, the data are fitted by exponential functions.

Despite the probably high error of our results (lets determine it as ± 2 nm instead of ± 1 nm), another positive fact is the agreement of results from both samples in usable area and also quite good (taking into account errors) agreement with previously published spin relaxation length in copper measured also using THz emission by Seifert *et al.* [11]. Their results were $\lambda_{rel} = 4.0$ nm and were not to much affected by changing conductance of the sample, because their measurements were done on samples with additional copper wedge on the top which may lead to constant conductivity everywhere on the sample but makes it harder to measure the speed of the electron transport presented further in this thesis (and never before in the literature). A small discrepancy is that Seifert *et al.* did not report any changes of spin memory loss. This can be because of different fabrication method used for sample growth which can affect the interfaces a lot, so does the spin memory loss [28].

Both our and Seifert's measured spin relaxation lengths are significantely smaller than the known spin diffusion length in copper, which is approximately 500 nm [14]. That is the reason to expect different type of spin polarized electron transport in spintronic emitters than the casual diffusive one described by the Drude model and our motivation to study the speed of this transport.

3.2 Out-of-plane spin current: Speed of propagation

Another goal, we have set to reach using data of THz emission from samples 1 and 2, is to reconstruct the exact speed of propagation of spin polarized electrons in copper during THz emission proces. Thanks to the high time resolution of measured waveforms (specially those detected by very thin crystals), we may be able to see timeshifts of all waveforms depending on the thickness of copper on actual place of emission. As written in the theory part, by measurement of this shifts, we would know the electron motion speed also during classical spintronic process of THz emission and that means also during ultrafast demagnetisation.

3.2.1 Evaluation of THz waveform's shifts

For this evaluation we start from the same measured datasets as shown in Fig. 3.5 a) and c). The other two datasets used for evaluation of spin relaxation lengths were enough precize to evaluate the changes of amplitudes from them but they were not measured for such a long time to have enough low noise to evaluete the shifts from them.

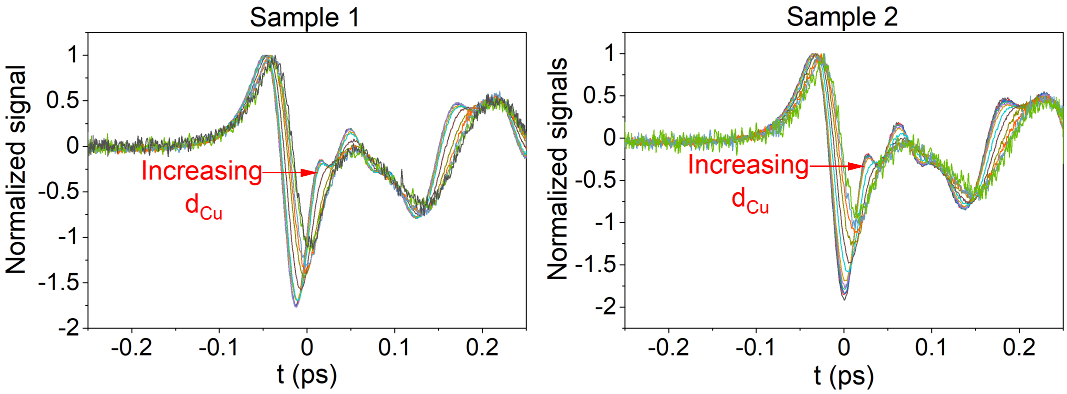

Figure 3.8: Waveforms emitted from sample 1 and 2 normalized on maximal value. Clearly observable temporal shifts with increasing d_{Cu} are indicated by red arrows. Increase of noise level is due to larger attenuation of THz waveform at positions with larger G.

As we see in Fig. 3.8, clearly there is an observable timeshift between the individual waveforms normalized on their maxima in both samples. Question is how to evaluate these shifts precisely. We tried four different methods. Two simpliest were based on the monitoring of the position of the maximum and of the minimum of THz waveform. In the next method, we determined the position of maximal decrease on the waveform. Firstly, we cut the part of the waveform between maximum and minimum, then we slightly smoothed these curves using Matlab function smoothdata [51], made a derivation, fitted polynom to the a bit noisy derivated curves and find the extreme of these polynoms. The last used method was a bit more abstract and that is the reason why we demonstrate it step by step in Fig. 3.9. It is the method of reconstruction of time shifts of curves from the phase of their spectrum. If we do the Fourier transform of a THz waveform, we get the THz spectrum from the absolut value like in Fig. 3.9 a), but we can also express the argument of spectra pictured in Fig. 3.9 b). This argument ”jumps” each time when it reaches a multiple of 2π but it is easy to strighten these jums by ading the propriate multiple of 2π after each jump (as in Fig. 3.9 c)). The argument of Fourier amplitudes is $2\pi ft$, where t is time and f is frequency. So if we fit the strightened arguments by a linear function $g(f) = q \cdot f$ for each waveform as in Fig. 3.9 d), the slope q after dividing by 2π gives us the absolut time location of each waveform.

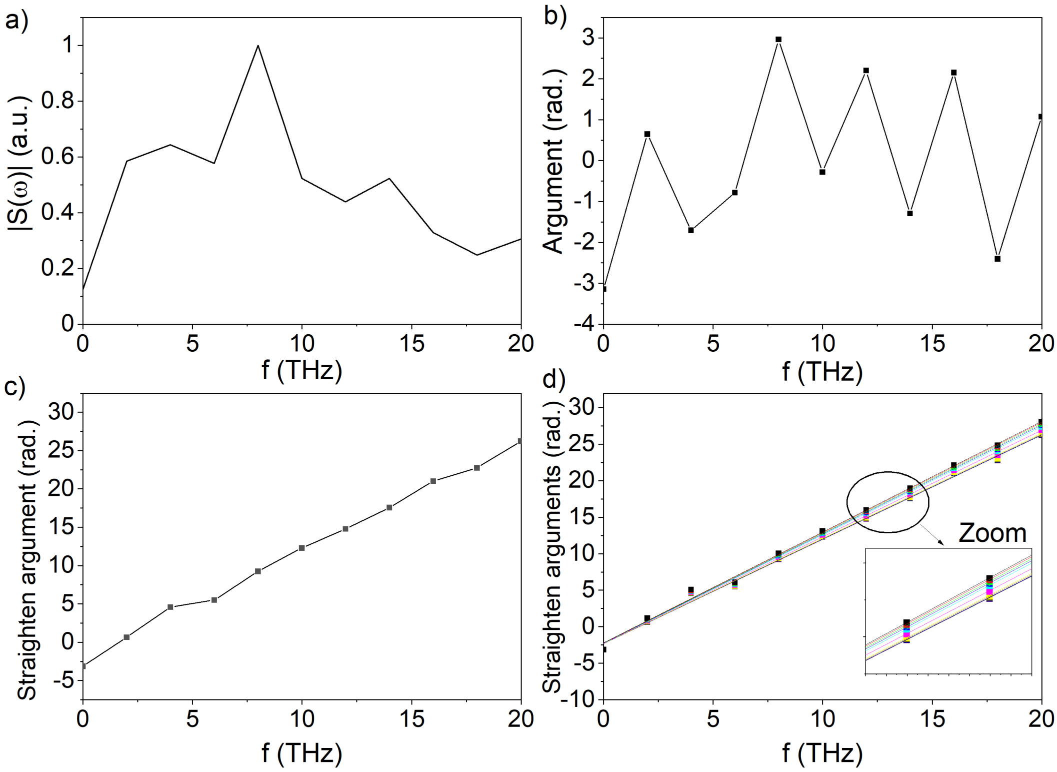

Figure 3.9: Step by step demonstration of reconstruction of timeshifts from Fourier’s phase. Firstly, it is made the Fourier transform of waveforms is calculated - the absolut value of it a) give us the spectrum. The argument of it b) has to be strightened, as shown in c), and from the slopes of linear functions fitted on all dataset d) we infer the timeshifts.

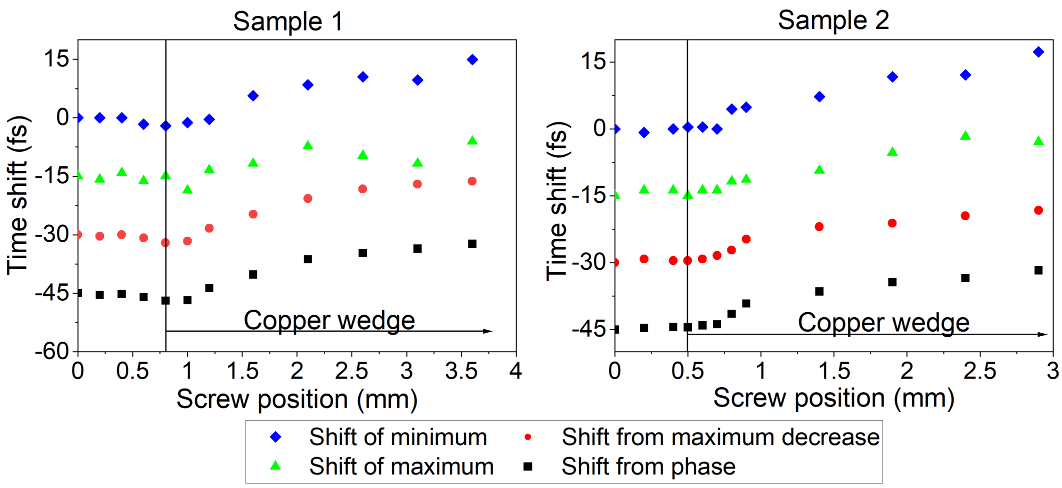

Figure 3.10: Times shifts evaluated on both samples by all 4 methods. The start of copper wedge is indicated by the vertical line. The shifts of individual datasets are vertically shifted by multiples of -15 fs for clarity.

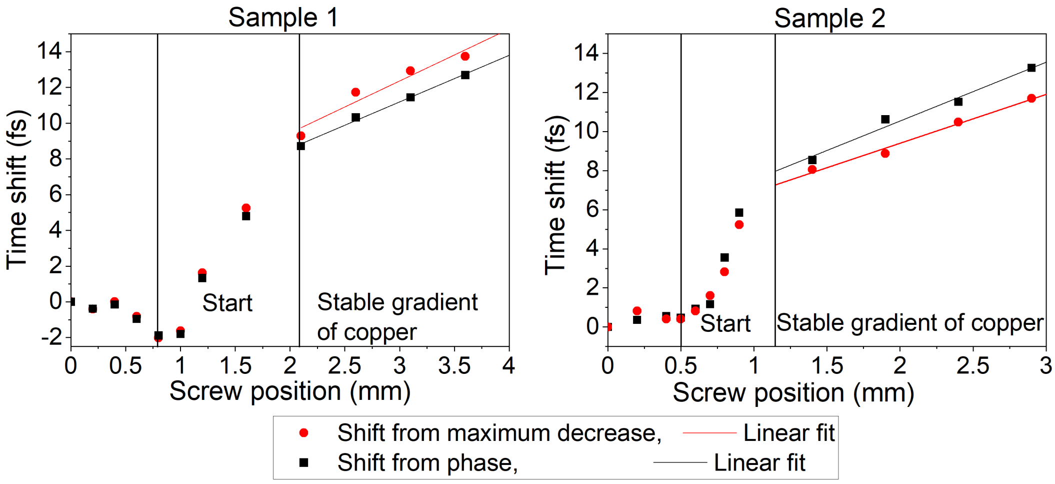

Figure 3.11: Timeshifts evaluated by the two best methods (from phase and from position of maximal decrease). The data on sample 1 are corrected on the shifts on the referential position. The area of beginning of the copper wedge with undefined gradient is marked by word Start. In the area of stable gradient the data are fitted by the linear functions.

Using these four evaluation methods, we reached timeshifts ($t - t_0$, where t_0 is the temporal position of first curve at screw position = 0) summarized in Fig. 3.10. Based on the evolution of amplitudes in Fig. 3.5 b) and d) and on the change of slope in the intercepts of these data, we marked the point of begining of the copper wedge. The shifts of multiples of -15 fs in y direction were added to individual datasets to have more clear picture. On both samples we can recognize that the evaluation method based on finding the position of maximal decrease and from phase are more precise (there are less oscillations in data).

Based on this obsevation, we made detail pictures of timeshifts evaluated by the two better methods and shown them in Fig. 3.11. In both cases there are clearly visible the points where the wedges begin, corresponding to the screw positions marked in Fig. 3.5 b) and d). Then, there are the areas, similar to graphs from the evaluation of spin relaxations, where the wedges have undefined thickness and a bit unexpected behavior (marked by word Start). The lines showing the end of this area are located in the same places (corresponding to the copper thickness of 4 nm) as in the evaluation of spin relaxation lengths in Fig. 3.6. Finally, there are areas where the gradient of copper is stable and we can determine the spin current speed from the data located here. For this reason, the points at this area were fitted by the linear function to emphasize the linearity.

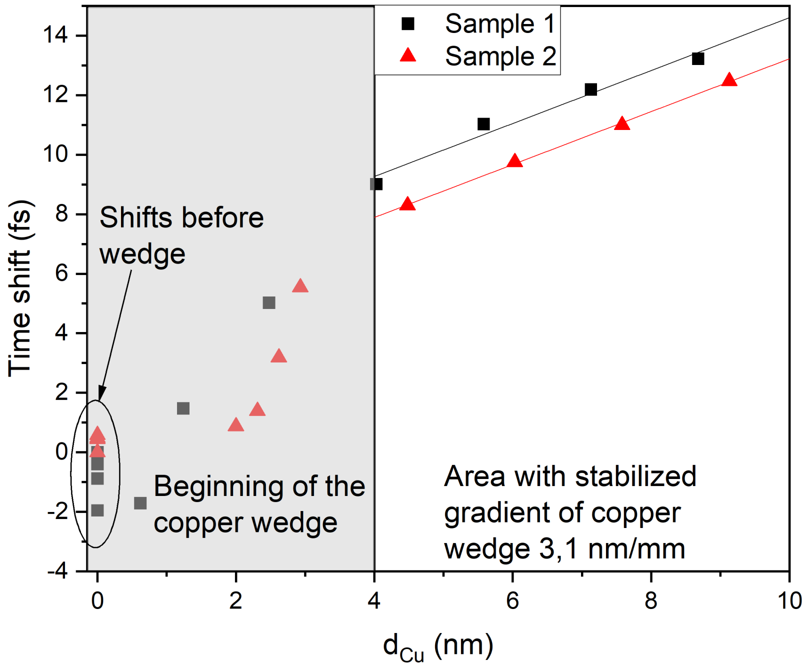

Figure 3.12: Timeshifts averaged from two best methods on both samples as a function of copper thickness, fitted by a linear function in the area of stable copper gradient. The area of beginning of the copper wedge has a grey background, all the shifts measured in front of the estimated begining of the wedge are plotted at position $d_{Cu} = 0$.

Finally in Fig. 3.12, there are timeshifts averaged from two best methods (from shifts of maximal decrease and from phase) on both samples as a function of d_{Cu}. The slopes of fitted lines are (0.89 ± 0.1) and (0.89 ± 0.02) fs/nm for sample 1 and 2, respectively (errors are just statistical errors of linear fits). The grey area, indicating the unusable data from the begining of the wedge, is the same as in the case of evaluation of the spin current relaxation lengths. Also, all the shifts of THz curves emitted from the bilayer before the estimated start of the copper wedge are there plotted at the $d_{Cu} = 0$ position. This might be interpreted as the absolute scatter due to other sources (thickness variation of substrate, imperfectness of the sample near to the wedge, ramdom drifts etc.). The relative vertical offset of the dataset in the usable area is there probably again only because of the problematic estimation of the beginnings of the wedges. Another discrepanccy is in the fact that the increase of shifts per d_{Cu} appears to be up to twice as large at the beginning of the wedge (gray area) as in the stabilized area. This would agree with a much faster decrease in amplitude on sample 2 in the grey zone in Fig. 3.6.

So, we have an incredible agreement in the slopes of the fitted lines, on the other hand, the sizable variation in front of the wedge and unexpected larger slope in the grey area. In addition there is the vertical shift in the usable area between both data sets. That makes the estimation of the error complicated but for now let's consider the slope to be 0.89 fs/nm without immediate estimation of the error and let's discuss the possible origins of these shifts.

3.2.2 Speed of electron transport in STE

The question is whether the shifts are really given by the time needed by spin polarized electrons to traverse the copper spacer.

Additional shifts can be caused, for example, by the long term temporal instability of the THz pulses (for example because of not perfectly stable dry air flow in flowbox). For this purpose, we conducted measurement on sample 1 in a way that after each measured curve on copper wedge we measured a new reference curve in front of the wedge. The shifts between the subsequent reference curves were then subtracted from the relative shifts of curves measured on the wedge. We used this analysis for measurements on sample 1 (already applied to the data in Fig. 3.12), but the data from sample 2 were not corrected in this way. We observed that this random variation of points on $d_{Cu} = 0$ is not large enough to explain the observed systematic increases in delay in the rest of the graph and the uncorrected measurements in sample 2 gives the same resulting slope of delays. The effect of these fluctuations is therefore not decisive for our interpretation.

Another reason which could affect the evaluation of the shifts is reshaping of the waveforms caused by a change of the phase in Gaussian beams (see equations 2.11, 2.14) around the waist position - so called Gouy shift. In the case of THz pulse emitted from the sample which is placed near the optical focus, even a slight motion with the emitter in z direction can cause shifts of the THz waist position which can propagate through the setup and affect the final Gouy phase at the place of the THz detection. Such artificial phase shift can be false interpreted as a real time shift of curves. In our case, the emitting sample was placed in the holder on a translation stage under a slightly oblique incident angle to prevent the back reflections into the laser oscillator. So, such accidental shift of the emitter in z direction can happen when translating the sample in x direction to scan the wedge.

Firstly, we have to determine the maximal possible shift of the sample in z direction during the measurements. For this purpose, we made a scheme in Fig. 3.13 a). The back reflected optical beam (red line) was pointing on iris in the distance $\Delta z \approx 1$ meter back in the optical path on the place $\Delta x \approx 1$ cm away

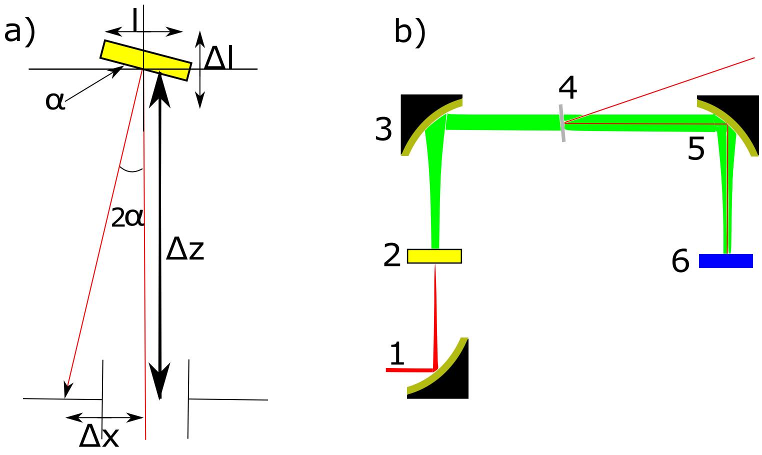

Figure 3.13: a) Scheme for estimate of the shift of the sample in z direction and b) the optical path which must be tranversed by THz radiation from emission from STE (2) to dection (6).

from the center of the iris. From this approximate geometry, it can be estimated the angle of reflection as $2\alpha = 0.6$ ° which is two times bigger than the sample rotation angle α. In both cases, we scanned aproximately 3 mm of the sample laterally (in x direction) when being on the copper wedge, so the shift l in Fig. 3.13 a) is maximally 3 mm. From estimated angle $\alpha = 0.3$ ° and lateral shift l, we can estimate the maximal possible shift in the z-axis (marked in Fig. 3.13 a) as Δl) as 15 µm.

We have created the scheme in Fig. 3.13 b) for easy to follow the simulation method. We assume that the sample at position 2 was (with optical beam pointing on the place of the copper wedge beginning) placed so that the emission came from z-position correspoding exactly to the optical waist. Then, the scanning by 3 mm laterally on the copper wedge induce a z-shift of the emission point by 15 µm away from optical waist, so the most extreme case assumed. The original optical beam had (in Fig. 3.13 b) at position (1)) the full width at half maximum of intensity ($\mathrm{FWHM}_{I,opt} = \sqrt{2\ln 2}w_{I,opt}$, where $w_{I,opt}$ is the radius of optical beam from eq. (2.11)) equal to 1 mm and was collimated. Then, there was a lens with a radius 2.5 cm and focus length 7.5 cm, focussing the beam to the place of THz emission (2). There, according to the modelling, the $\mathrm{FWHM}_{I,opt}$ is aproximately 25 µm. Using the scripts from [52] for numerical modelling of the Gaussian beam propagation described in section methods, we can construct the q-parameter at the place of THz emission. Now when THz radiation is emitted, we assume the change of parameter w from the optical intensity to the one describing directly electrical field of emitted THz beam as $w_{E,THz} = \frac{w_{I,opt}}{\sqrt{2}}$ (as the emission is the second order non-linear process) and at the same time change from the optical frequencies around 790 nm to the THz ones. Both these variations change also the Rayleigh length, so the q-parameter. With the new q-parameter, we continue with modelling of the propagation through the system towards 7.5 cm distant collimating lens at position (3) (same as the first focusing one), then (intentionally exaggerated) 1 meter propagation of collimated beam through the free space (the traverse through the thin silicon wafer did not change the parameters), again

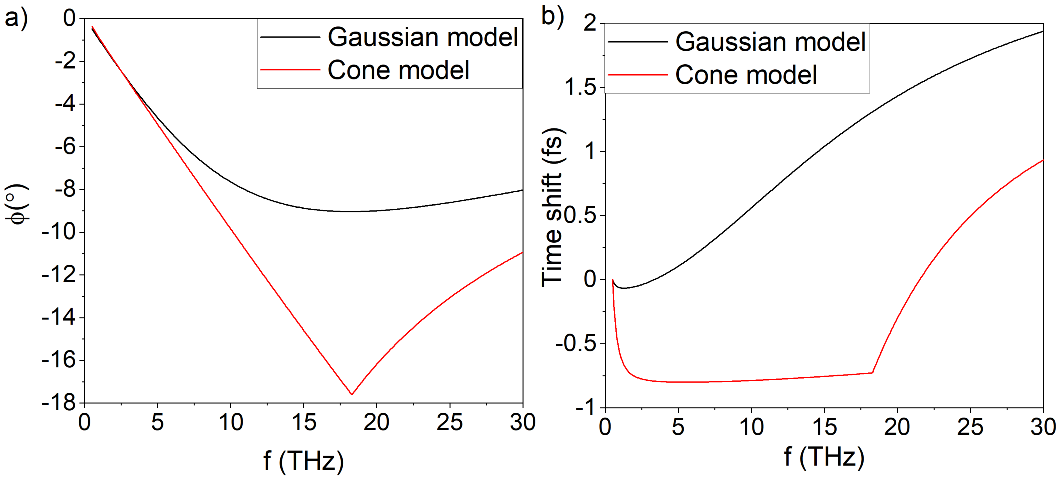

Figure 3.14: Maximal possible change of Gouy phase ϕ (deg) a) and caused timeshifts of THz waveforms b) at the position of detection between z-shifts 0 and 15 µm. Numerical simulation made with scripts from [52] for case of Gaussian aperture model (circular aperture is replaced by a Gaussian aperture with equal power transmittance vertically to a normally incident plane wave) and Cone model (hard circular aperture that removes all THz field with divergence larger than the equivalent numerical aperuture, i. e., high-pass filtering in THz spectrum)

focusing at position (5) and finally observing the Gouy phase at the fixed position of detection (6). Now, we repeat all this modelling with the sample shifted by 15 µm from the optical waist position. This, according to our model, change the position of THz emission waist at position (2). Then, we can observe the propagation of this z-shift also to the position of detection. Here, we again reconstruct the Gouy phase from q-parameter (following eq. (2.13) and look at the change for situation with z-shift = 0 and 15 µm with spectral resolution from 0.5 to 30 THz. This is shown in Fig. 3.14 a). The two curves show us modelling with (i) perfect Gaussian apertures when passing through lens and with (ii) the consideration of cutting off the low frequencies as they are more divirgent than the lens can catch (cone model). From the difference of the Gouy phase at the position of detection, we can easily reconstruct the apparent time shift as

$$\delta t = \frac{\phi}{\omega_{THz}},$$

where ω_{THz} is the frequency of the THz pulse. These results for both methods are plotted in Fig. 3.14 b). In this figure, we can see that the experimentally measured shifts cannot be definitely caused by the Gouyshift only - even in the case of 30 THz it can cause maximally 2 fs apparent shift for the Gaussian aperture model and less than 1 fs shift for the cone model. Moreover, the argument is equal to $2\pi\delta t \cdot \omega$ in Fig. 3.9 and if there was a Gouy shift, then $\delta t = f(\omega)$, so the argument would be nonlinear which we do not observe in Fig. 3.9. We note that for evaluation of shifts from phase we use frequencies only up to 20 THz, where the maximal Gouyshift is around 1 fs. So, the Gouy shift affects, if at all, the results only marginally.

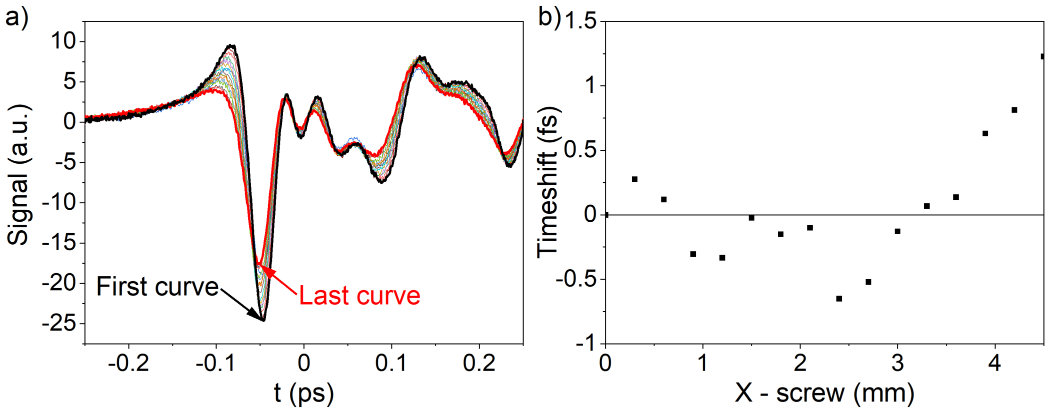

Figure 3.15: a) Waveforms emitted from sample 1 from CoBeB(2)/Pt(2) only, thick red and black curves are emitted from places 4.5 mm apart. b) timeshifts of these curves evaluated from phase

Last possible reason for additional timeshifts, that the author can think of, is the unstable thickness of the substrate. As the generation beam has to pass through it, it can again cause additional temporal shifts. For this purpose, we have measured also shifts of waveforms emitted from pure CoFeB(2)/Pt(2) deposited next to the wedge on the sample 1 (shown in Fig. 2.6 on the top). This measurement brought us surprising result, because the waveforms (shown in Fig. 3.15 a)) were quite deformed when the emission position was scanned over the bilayer. But the more abstract evaluation of shifts from phase shown in Fig. 3.15 b) did not show any bigger systematical shift (maximal deviation from original time position is ≈ 1.2 fs). Because there is no reason for such big reshaping of THz waveform from CoFeB(2)/Pt(2), we have to suspect that the bilayer here is probably demaged (possibly the interface quality is inhomogenious) and these measurements are a bit spoiled. Anyway the systematical change in substrate thickness is, based on these results, probably not there and the fluctuations are too small and irregular to explain our findings above.

The final argument confirming that we have measured timeshifts caused by the time of electron transport through copper is the evident and sudden rise in shifts at the beginning of the wedges and the fact that the slopes of their increase from both samples agree together excellently.

After all the argumentation, we can infer the averaged slope 0.89 fs/nm and calculate the velocity of the spin polarized electrons as an iverse value of this slope. The velocity is then $(1.1 \pm 0.5) \cdot 10^6$ m/s. We intentionally increased the error so that it refers to all the previous argumentation about other possible sources of the shifts, about shifts of curves on default positions and possible other inaccuracies.

The Fermi velocity in copper is, according to Zhu *et al.* [17] and [36], $1.57 \cdot 10^6$ m/s. Using their theory, the wavefront should move at speed $c = v_f/\sqrt{3} = 0.91 \cdot 10^6$ m/s. This is an excellent match with our value $c = (1.1 \pm 0.5) \cdot 10^6$ m/s, so, despite the error of our method, we are sure that the transport during UDM and the spintronic emission is ballistic, as Zhu *et al.* predicted.

3.3 Out-of-plane spin current: Relaxation time

Lets now have a look on the spin current lifetime. Using basic equation for spin current relaxatin length $\lambda_{rel} = c\tau_{rel}$, (using previous results $\lambda_{rel} = (5 \pm 2)$ nm and $c = (1.1 \pm 0.5) \cdot 10^6$ m/s) we can get life time of spin current yielded from our results as $\tau_{rel} \approx 4.6$ fs.

Now, we start from an idea that τ_{rel} is given by spin relaxation time τ_s and also by the relaxation of ultrafast current. From the experiments above, it appears that the spin current is ballistic, so the second relevant time would be the scattering time τ from Drude model (eq. (1.8)). τ_{rel} will be determined by the smaller of these two ($1/\tau_{rel} = 1/\tau_s + 1/\tau$). Since we expect $\tau_s \gg \tau$ in metals (spin is randomized every 10-100 scattering [14]), our hypothesis is that $\tau_{rel} \approx \tau$ if the spin transport if really of ballistic nature.

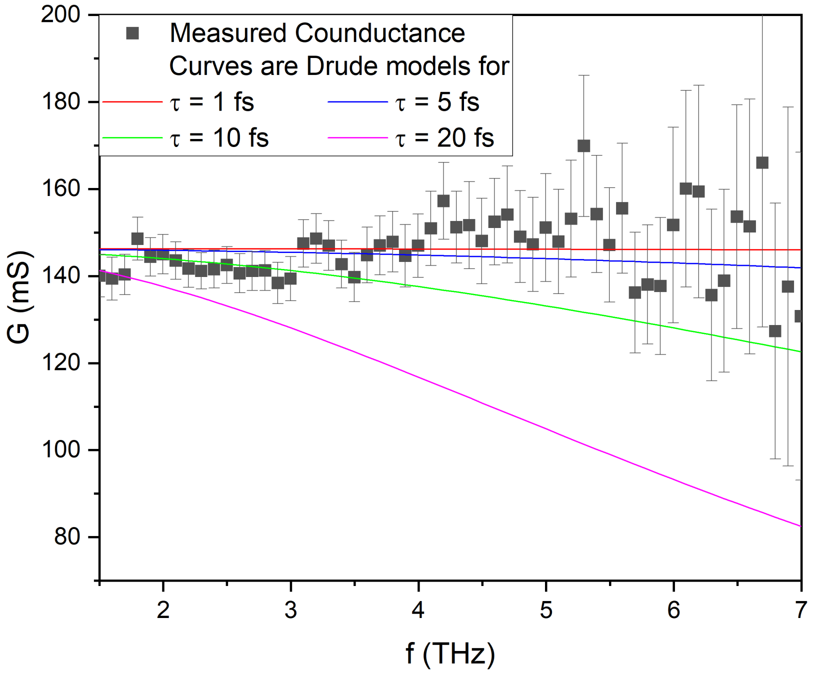

Figure 3.16: Conductance of sample 2 measured for $d_{Cu} \approx 11.5$ nm (compare the mean value of 146 mS with the last point in Fig. 3.4), together with calculated curves from the Drude model for indicated relaxation times τ. The errors are estimated from the white noise in spectra measured through sample and through substrate.

This hypothesis can be verified experimentally by the measurement of conductance on sample 2 shown in Fig. 3.4. If we consider the conductance from this figure at the position of thickest copper ($d_{Cu} > 10$ nm there), it is totaly dominated by the conductance of the copper layer. In Fig. 3.16, we show the spectrum. The curves in this figure are calculated from the Drude formula 1.8 with different τ (only instead of σ_0 we use there G_0 for easier comparison with Fig. 3.4). We use a calculation for a given τ instead of fitting because of the nearly constant frequency dependence which makes the fitting unreliable. The errorbars are calculated from estimation of white noise in originally measured spectra.

We can see that the red and blue lines corresponding to $\tau = 1$ and 5 fs can be both used as a good approximation of measured data (with consideration of the errorbars and dispersion of datapoints). But already the green curve for $\tau = 10$ fs show us some deviation from the measured data and $\tau = 20$ fs is completely out of the trend.

So, despite the fact that we are not able to infer precise value of τ from Fig. 3.16, we have an upper bound of 10 fs for this value. It is fully consistent with expected $\tau \approx 4.6$ fs from our hypothesis and supports the notion that our spin transport is limited by the scattering time.

Therefore, we can finally conclude, using all our arguments, that the ultrafast spin current responsible for spintronic THz emission from our prototypical bi- and tri-layers is propagating with velocity close to expected v_f and limited spatially by the mean free path and temporally by the scattering time. All of this is consistent with the ballistic nature of spin current.

3.4 Out-of-plane spin current: Spectral filtering in copper

Last but not least, we can look at the spectra of signals emitted from copper wedges. We bring both datasets which we used for evaluating of spin current relaxations and the speed of ballistic electron transport shown in Fig. 3.5 a) and c). The normalized spectra reached from Fourier transform of these data are displayed in Fig. 3.17. The red dashed lines are the spectra of signals emitted from regions with $d_{Cu} = 0$ nm, the black dashed lines are the spectra of signals emitted on the places with the most thick copper spacers ($d_{Cu} \approx 9$ nm).

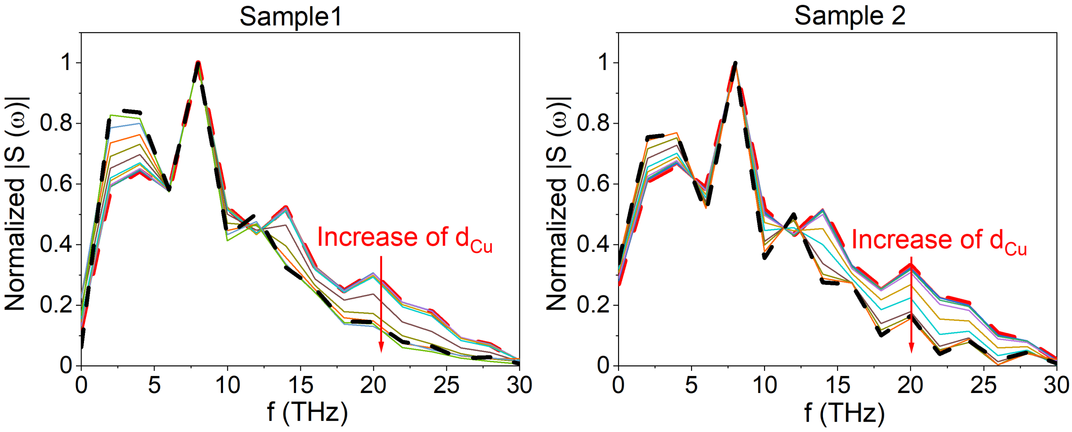

Figure 3.17: Normalized spectra of THz signals emitted from sample 1 and 2. The red dashed line is the spectrum of signal emitted from regions with $d_{Cu} = 0$ nm, the black dashed line corresponds to $d_{Cu} \approx 9$ nm.

It is nicely observable that the more thick the copper spacer is the larger is the low-frequency fraction in the spectrum. That means that there is a spectral filtering of higher THz frequencies during the proces of THz emission in regions with copper spacer.

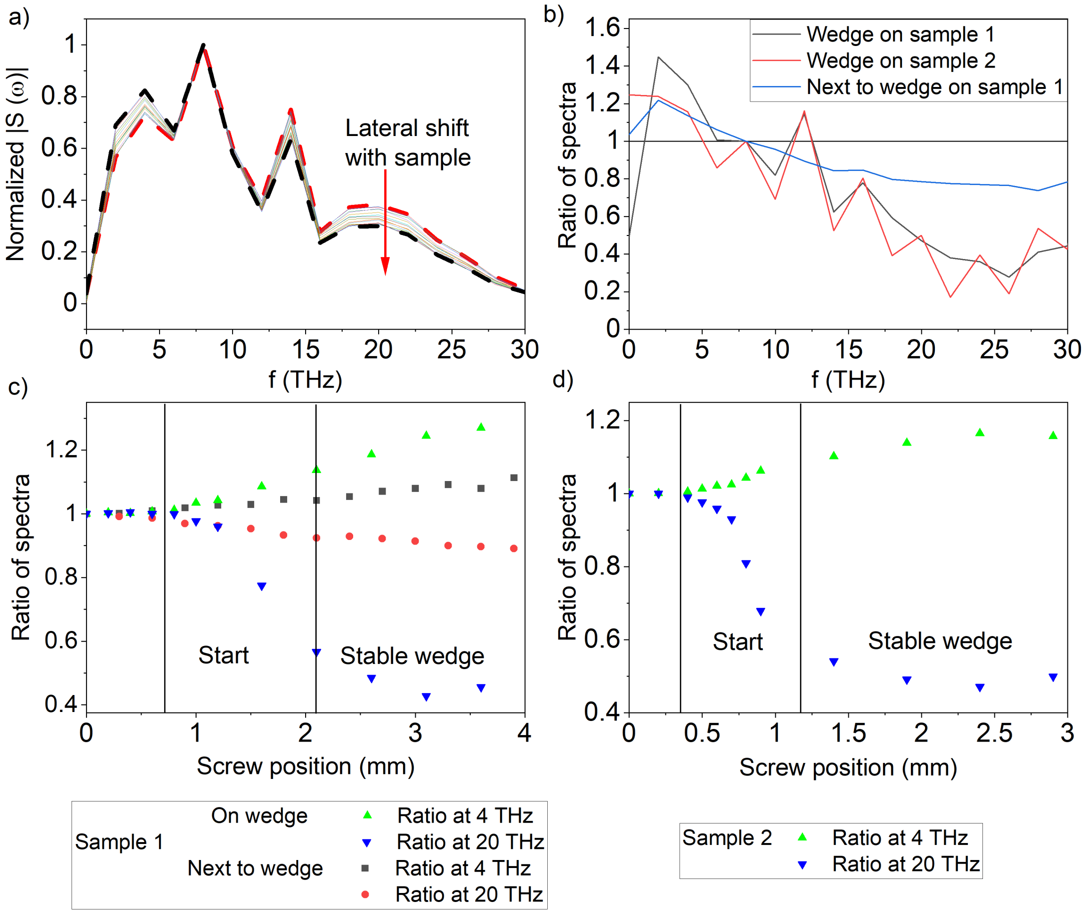

Figure 3.18: Summary figures describing properties of spectral filtering in copper. a) Normalized spectra of THz signals emitted from sample 1 next to the wedge (on bilayer), red and black dashed lines show the spectrum of first and last curve when moving laterally. b) Ratio of last and first curve from spectra in Fig. 3.17 and 3.18 a) (dashed curves in these figures). c) and d) Ratios of datapoints from spectra in Fig. 3.17 and 3.18 a) at 4 and 20 THz as a function of screw position with marked places where the copper wedge starts (same as in Fig. 3.11).

To characterize the spectral filtering and their possible origins, we made Fig. 3.18. Firstly, we want to focus on the question whether this effect is connected to the copper spacer. When characterizing the timeshifts of waveforms emitted from sample 1 from bilayer region CoFeB(2)/Pt(2) only, we saw certain small changes of curve shapes too (see Fig. 3.15). For this purpose, we show the normalized spectra of these curves in Fig. 3.18 a). The filtration of higher frequencies on the last curve is evident. To compare this frequency filtering with the one observed on copper wedges, we made the spectral division: Last spectrum/First spectrum (First one is for $d_{Cu} = 0$ nm, Last is for $d_{Cu} \approx 9$ nm, or, on the reference bilayer, two spectra for $d_{Cu} = 0$ nm but after same lateral shift on the bilayer). This is shown in Fig. 3.18 b). It is visible that especially the filtering of higher frequencies is considerably bigger for the measurements on wedges.

To understand the origins of this effect even better, we did the ratio of the datapoints in Figs. 3.17 and 3.18 a) at 4 THz and 20 THz as a function of screw position. It is shown in Fig. 3.18 c) for sample 1 on the wedge and next to the wedge and in Fig. 3.18 d) for the sample 2 on the wedge (there was no bilayer next to the wedge where to measure this). The red and black points in Fig. 3.18 c) show us, that this effect of low-pass filter measured next to the wedge (on bilayer) is smaller than on wedge and linear in longitudinal shift. In comparison to that, this effect is, especially for high frequencies, much bigger and nonlinear on the wedges on both samples. It looks like the main spectral filtration is hapening in the areas of copper wedges beginings (previously in Fig. 3.12 and 3.6 marked by grey background, here by the word Start). Spatially in the case of sample 2 (Fig. 3.18 d)), it looks like there is really small spectral filtering further on the wedge (for $d_{Cu} > 4$ nm) and the effect occurs almost only in the area marked as start of the wedge.

To summarize these observations, we see the spectral filtering of higher frequencies when moving laterally on the sample when being on the wedge but also next to the wedge (bilayer, no spacer). Spectral filtration next to the wedge show us some probably globally changing parameter in the sample 1 (possibly the interface quality). Spectral filtration on wedges is much more significant (especially for higher frequencies) and it occurs mainly in the area with unexpected behavior previously discussed in sections about spin current relaxation length and speed of electron transport. For that reason, we believe that this effect might be associated mainly with the previously discussed spin memory loss processes in these areas. Another explanation could be the fact that the ballistic transport in copper according to Zhu and Schneider [17] should be dumpened more at higher frequencies. It is supported by the phenomenologically added constant term C_0 (indicating a slower, low frequency component) when fitting spin current relaxation time λ_{rel} in Fig. 3.6. However, with this samples it is hard to distinguish this effect from the others.

3.5 Inplane spin current: THz crystalline AMR

Now, we move from out-of-plane spin currents to inplane currents where the well known diffusive type of transport is realized. We will no longer need a multilayer samples, but a simple layer of metal and a THz transmission spectroscopy arrangement. These measurements will, unlike the previous ones devoted to out-of-plane currents, be measured in Prague in Karlov laboratory. We will focus on the first THz measurement of crystalline anisotropic magnetoresistence on cobalt-iron - Sample 3. As we described in the theoretical part, this material is unusual for its huge and anisotropic crystalline AMR and that is the reason for studying it.

3.5.1 First observation: magnetic-field-dependent modulation of THz transmitance

As the method of THz measurement of AMR [18] is quite recently reported and more complex relation of it to conventional electrical measurement is still not well established, we set the first goal to just measure THz transmitance through sample 3 placed in Halbach rotator over the full 365° rotation of magnetic field.

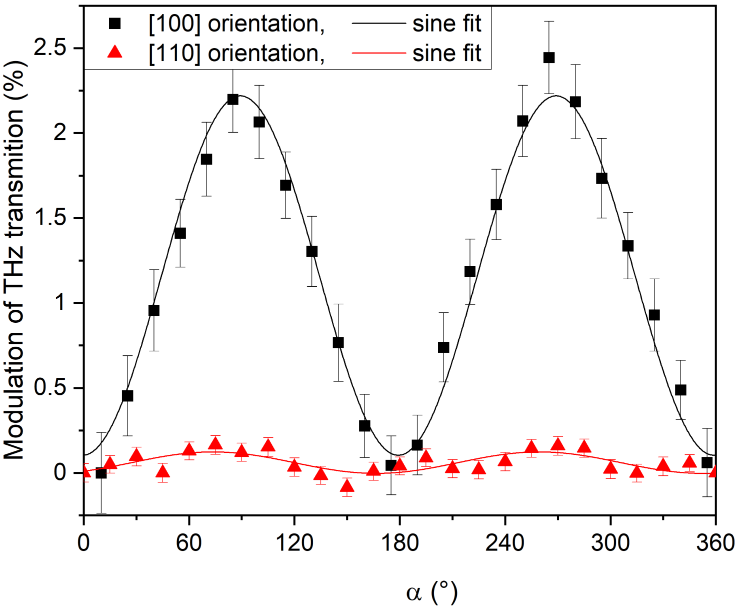

Figure 3.19: Modulation of THz transmitance through sample 3 as a function of the angle α between THz polarization and external magnetic field. Red points are measured for [110] orientation of sample along the THz polarization, black for [100] orienation. Fits $\propto \sin^2(\alpha)$ show us the clear modulation even in magnetization.

Firstly, we placed the sample in the THz beam so that the linear THz polarization was parallel to the crystalographical orientation [100] and, then, parallel to the orientation [110]. In this measurement, we only measured the THz field at maximum of THz waveform (i.e., at a fixed time-delay, see, for example Fig. 3.22 (a) with $t = 2.2$ ps). To prevent long term effects and have enough accurancy, we always measured 3 values at the curve maximum and rotate the Halbach rotator by 15°, until we did 32 or 245 full 360° rotations in case of [100] or [110] orientaion, respectively. The obtained modulation of THz transmitance in percents is shown in Fig. 3.19.

The errorsbars are calculated from the errors of averaged values (there was longer averaging in [110] orientation). Points are fit by a sine function to emphasize the nice modulation even in magnetization ($\sim \sin^2(\alpha)$, where α is the angle between polarization and magnetic field). Observed modulation is around 2.2 % for [100] orientation and smaller than 0.15 % for [110] orientation.

3.5.2 Contrast of AMR vs. crystallographic orientation: cross-crystalline AMR

Having an ecouraging message from nicely obsevable modulation of THz field transmited through sample 3 and showing an expected significantly higher modulation in [100] orientation of sample to THz polarization, we can start with a precise mapping of AMR.

To have a possibility to reconstruct the AMR contrast (following eq. (1.14)) from amplitudes of transmitted fields, we need to know the γ factor from equation (2.10). For the refractive index of air n_1 we use 1 and for a refractive index of MgO substrate we use (in used spectral range 0 to 2 THz) 3.1 [53]. Last needed coefficient is then the conductance G. For this purpose we measured the conductance of sample 3 the same way as before on sample 2. The steps of this method are shown in Fig. 3.3. In measured spectral range its value was again frequency-independent, so we get the single mean value $G = (6.7 \pm 0.2)\cdot 10^{-2}$ Ω^{-1}. Higher error in comparison to conductivities measured on samples 1 and 2 is there because of not so long averaging. The effect of conductance on AMR is not so strong and even the result with precision on one digit will be enough.

The γ factor yields 1.16±0.01 for the given values. The error is given from the error of measured conductivity.

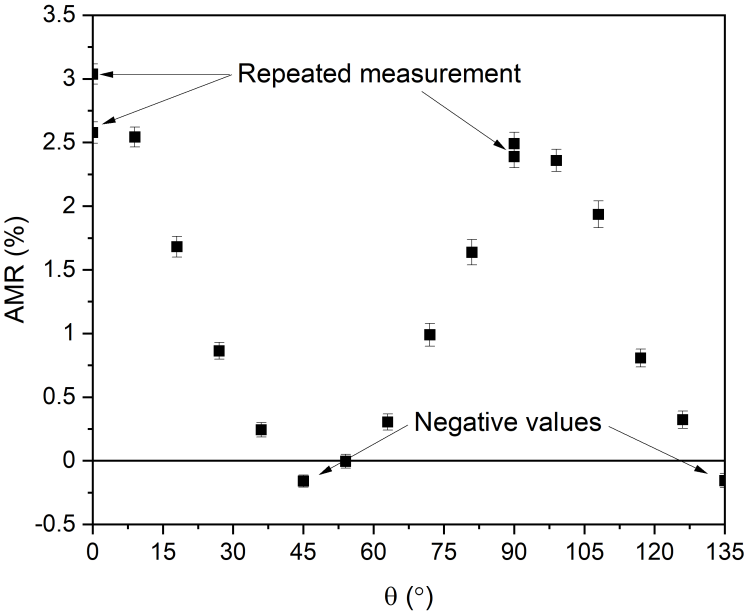

Figure 3.20: Measurement of contrast of cross-crystalline AMR in CoFe. Only the maximal values on THz waveform were measured for $\alpha = 0°$ and $90°$. Errorbars are calculated from errors of avereged THz fields. $\theta = 0$ corresponds to the THz polarization paralel to [100] orientation (see Fig. 1.4).

Now with known γ and the even (as expected) symmetry of AMR, we can express AMR contrast from eq. (1.14) only by comparing the values for $\alpha = 0$ and $90°$. Thus, it is possible to evaluate such AMR contrast for different current orientations (THz polarization) vs. crystallographic direction [100] from $\theta = 0°$ and 135°. Definition of angles describing AMR are the same as in the theory section, shown in Fig. 1.4. Using the equation (2.9), we got the data shown in Fig. 3.20.

Good news is the consistency of AMR contrast at $\theta = 0°$ and 90° corresponding to the orientations [100] paralel (respectively perpendicular) to THz polarization with the ≈ 2.4 % amplitudes in Fig. 1.5. Also the shape of the dependence of AMR on θ is similar. On the other hand, we did not get the fully symmetrical curves as Zeng *et al.* [19] and also the decrease of AMR contrast approaching the [110] orientation of crystal to THz polarization at $\theta = 45°$ is not so sharp. Moreover, at position $\theta = 45°$ and 135°, we got negative values. That led us to the idea that are probably some other unknown systematical errors in our measurements. For that reason, we repeated the measurement at 0° and 90° (plotted in Fig. 3.20). Especially the big discrepancy at 0° is showing us that some additional errors are included.

First thing, we could improve, was the automation of the sample rotation. Measurement on Fig. 3.20 was done so that we did long averaging of THz transmited field with polarization perpendicular and parallel to magnetic field and then we manually rotated the sample in the holder. By the implementation of electronically controled rotating sample holder we are able to rotate more often and get rid of the long term effects such as drifts of laser power or instability of THz pulse in time due to humidity variations.

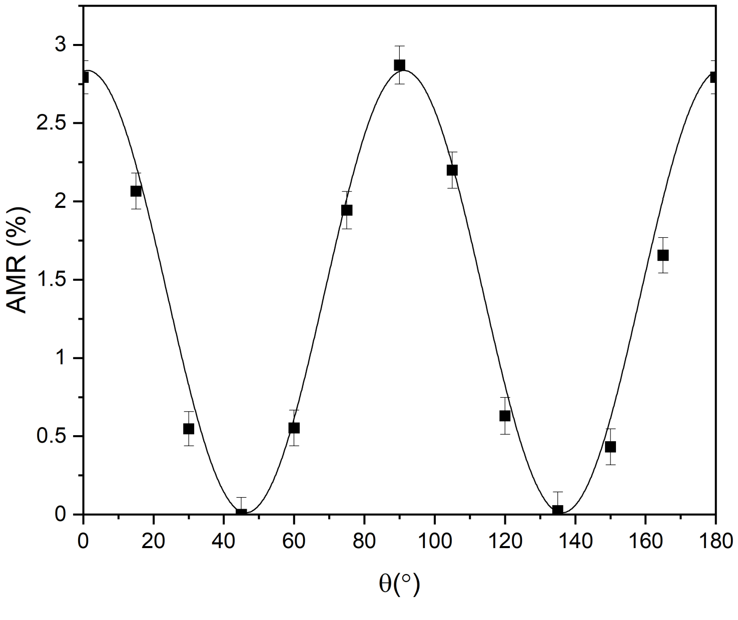

Figure 3.21: Improved measurement of cross-crystalline AMR on CoFe. Only the maximal values on THz waveform were measured. Errorbars are calculated ftom errors of avereged THz fields. $\theta = 0$ corresponds to the THz polarization paralel to [100] orientation. As a guideline for eye we fit there a sine function.

Also better placement of the sample in the THz focus so that the focus is centred in the middle of the holder, that we achieved this time, leads to the fact that by rotating we do not change the position on the sample, where the THz field is transmitted. This way we can get rid of the effects due to sample inhomogenities.

The results of same experiment after implementation of automatically rotating sample holder and more careful placement of the sample into the THz focus are shown in Fig. 3.21.

Good news is the fact that we got more symmetric shape of dependence of AMR contrast on θ and the negative values at $\theta = 45°$ and 135° disappeared. As a guide for an eye we used a sine function which shows us that the shape of dependence is definitely different from the one by Zeng *et al.* in Fig. 1.5, which looks like absolut value of sine. Also now we are more convinced that the contrast of AMR at "AMR easy directions" measured by THz radiation is a bit higher ($\approx$ 2.8 %) than the 2.4 % by Zeng *et al.*

3.5.3 Spectral dependence of intrinsic AMR

Another advantage of measurement of AMR using THz radiation is the possibility of having the spectral resolution. In order to find out if there is nontrival spectral dependence of AMR for different crystallographic orientations, we determined the AMR by measuring full THz waveforms for $\theta = 0°$, 22° and 44°. We intentionally did not choose the case of $\theta = 45°$, because the previous measurements show us that there could be no obsevable AMR and we wanted to measure a nonzero signal.

In Fig. 3.22 a), there are shown the transmitted waveforms for magnetic field parallel and perpendicular to THz polarization in case of sample orientation [100] ($\theta = 0°$). By the substraction of these two curves, we get again a waveform, which is quite similar to the original one as shown in Fig. 3.22 b). Therefore, already now we can expect no significant spectral features. We got again approximately 2.5 % modulation of signals similar to that in Fig. 3.19. In Fig. 3.22 c), there is shown the spectrum of the substracted curve with marked usable spectral range in Prague laboratory. Finally, the division of the spectrum of the substracted curve and the original curve give us, after multiplying by the γ factor, the AMR with spectral resolution. This is shown for all three orientations of the sample in Fig. 3.22 d). In spectral range from 0.2 to 1.6 THz we do not see any clear trends or features - the values are practically constant and the horizontal lines show the avereged values. Errorbars were, same as in case of conductivity measurement, estimated from white noises of spectra of original curves and substracted curves above 2 THz. Again, we see there slightly higher AMR for [100] orientation ($\approx$ $2.9 \pm 0.1\%$) than Zeng *et al.* reported. That is in terms of errors in agreement with the measured values in Fig. 3.21.

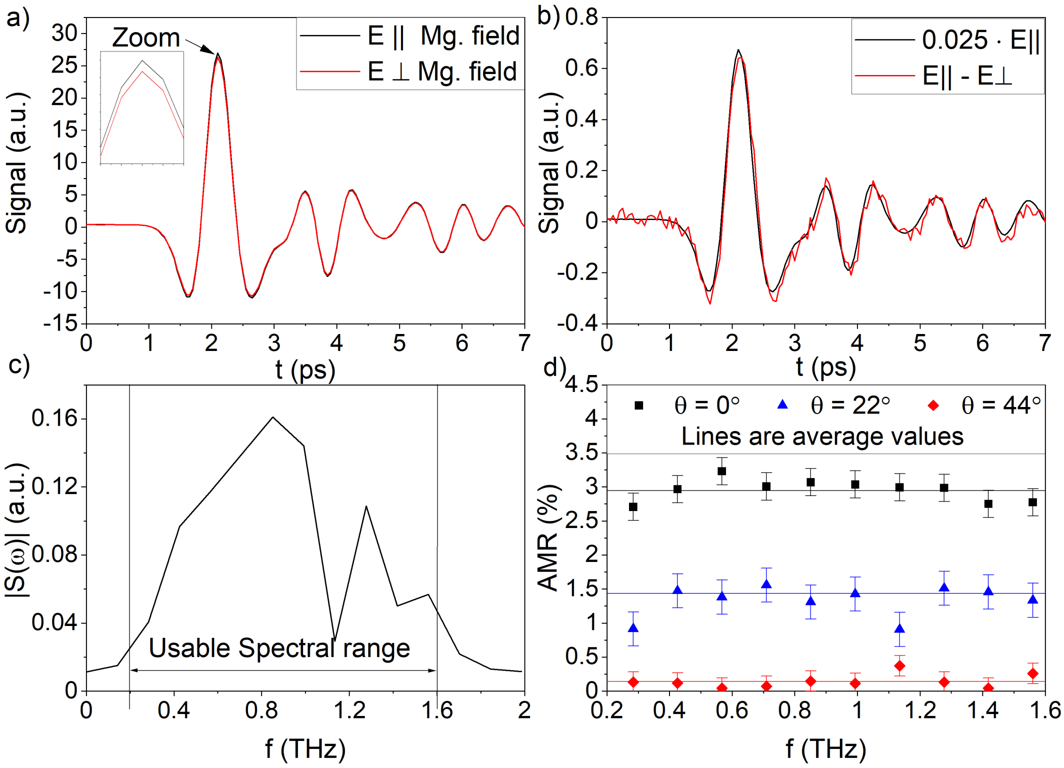

Figure 3.22: Steps of evaluation of AMR with spectral resolution and resulting AMR for three crystalographical orientations $\theta = 0°$, $22°$ and $44°$. a) Measured transmitted THz waveforms in cases of paralel and perpendicular magnetic field to the THz polarization, b) substraction of these curves overlaped by the rescaled original curve, c) spectrum of substracted waveform with marked usable spectral range and d) the final AMR for all three orientations with horizontal line showing the average value. The errorbars were estimated from white noise of spectra.

3.5.4 Discussion on THz measurement of AMR

In the previous two sections, we measured for the first time the crystalline AMR in the THz region and verified that it has a similar dependence on the crystallographic orientation as electrical measurements [19]. The smaller steepness and "blur character" of the dependence (in comparison to character in Fig. 1.5 looking like absolut value of sine) may be due to imperfect monocrystallinity. While DC measurement is sensitive only to the size of the halbar, we average over 0.5 mm (THz spotsize). There could be grains with slightly different rotations. The AMR contrast in "AMR easy axis" in this work was around 2.8 to 2.9 %, which is aproximately 15% higher than in electric measurements. We can explain this only by another systematic error in our measurement. We used γ factor calculated from G measured in [100] direction, but also G is in this sample a bit anisotropic. Moreover, each sample can be fabricated slightly different and for example the error in determining the thickness also affect the γ factor. In addition, small discrepancy in the exact size of the AMR contrast in comparison to electric measurement was observed also in the very first THz measurement of

AMR [18].

The constant character of the spectra in Fig. 3.22 can be interpreted as the fact that at these frequencies the energy of photons is still quite small and electrons are only very slightly shifted from the Fermi level, similar to DC exp. So, in the band structure calculated in [19], we are still close to anti-crossings as in DC transport. In order to measure the impact of larger excitations and thus verify the anti-crossing hypothesis, or check the intrinsic (scattering-independent) vs. extrinsic (scattering-dependent) nature, we would have to go to higher frequencies (probably tens of THz) or optical frequencies. These higher THz frequencies are not available in Prague laboratory nowadays, but the optical measurements are about to be done soon.

For high THz frequencies, it is necessary not only to develop a laser system and a suitable setup with a much shorter excitation pulse, but also move to the reflexion geometry. That is one of my plans what to do during my PhD. studies, to put into operation this. Such a measurement could then, analogous to the [18], also access the effect of scattering mechanisms on this type of AMR.

Conclusion

The aim of this work was to measure the two types of transports. Firstly, there were the out-of-plane spin currents manifested in the spintronic THz emitters where we wanted to ultimately and explicitly decide a fairly discussed question what kind, diffusive or ballistic, of spin current plays the role. Then, we wanted to measure the inplane transport, especially, we wanted to use THz transmission geometry for the historically first measurement of the crystalline AMR in the THz frequency range.

Firstly, we measured and discussed the properties of out-of-plane spin polarized electron transport during the spintronic process of THz emission. We were able to approximately reconstruct the spin relaxation length in copper from amplitudes of THz waveforms emitted from spintronic emitters with variable thick copper spacer as $\lambda_{rel} = (5 \pm 2)$ nm. From the timeshifts of THz waveforms, we have reconstructed the speed of ballistic spin-polarized electron transport as $c = (1.1 \pm 0.5) \cdot 10^6$ m/s, which is perfectly consistent with the theoretical predictions in [17].

From spin relaxation length and speed of the transport, we calculated the life time of spin current as $\tau_s \approx 4.6$ fs. We introduced the hypothesis that τ_s is comparable to the scaterring time from Drude model τ which was then experimentally confirmed by the flatness of the conductance spectrum measured in a sample on place dominated by copper conductance.

We further observed the high frequency filtration in spectra of THz waveforms emitted from samples with thicker copper spacers. We hypothesized the possible origins of this effect to be mainly caused by the changes of spin memory loss on the beginings of the copper wedges, but also partially by the global changing quality of interfaces in whole sample and possibly the effect of high frequency filtering during ballistic transport predicted by the theory [17].

Another part of this thesis was devoted to THz measurement of crytalline AMR on CoFe. We demonstrated the usability of this contactless method and also possibility of observing the spectral dependence of AMR.

The contrast of AMR in "easy axis" was around 2.8 to 2.9 %, which is a bit higher value, than the one measured fully electrically in [19]. We observed sine-like modulation of AMR contrast when rotating the sample and changing crystallographic oriantation which is again slightly different from results in [19], but it can be explained by the averaging on bigger area (with THz spot), than by the DC measurements and the possible grain structure of the sample. It looks like there is no AMR under the AMR "hard axis" (shown in Fig. 3.21). In measured low THz spectral window, we did not observe any spectral changes in AMR with sample under different orientations.

Our results can help to better understand and potentially optimize the spintronic emittrs of THz radiation, which are already becoming a common part of THz laboratories. Moreover, we contributed to understanding of the spin polarized electron transport in processes of ultrafast demagnetization. We demonstrated the possibility of THz measurements of crystalline AMR in the Prague laboratory and in general.

This show us also the possiblities of improvement of our setup by introducing also high THz frequencies and reflection geometry, which can both help us in further studies of AMR not only in CoFe, but also in antiferromagnets or altermagnets [54]. With these projects and tasks I would like to continue during my further scientifical research.

Bibliography

[1] S. Bandyopadhyay and M. Cahay. *Introduction to Spintronics.* CRC Press, Hoboken, 2008.

[2] S. M. Yakout. Spintronics: Future technology for new data storage and communication devices. *Journal of Superconductivity and Novel Magnetism*, 33:2557–2580, 2020.

[3] T. Jungwirth, X. Marti, P. Wadley, and J. Wunderlich. Antiferromagnetic spintronics. *Nature Nanotech*, 11:231–241, 2016.

[4] M. M. Waldrop. More than moore. *Nature*, 530:144, 2016.

[5] A. S. G. Andrae and T. Edler. On global electricity usage of communication technology: Trends to 2030. *Challenge*, 6:117–157, 2015.

[6] S. Blügel, D. Bürgler, M. Morgenstern, C. M. Schneider, and R. Waser. Spintronics - from gmr to quantum information. *Lecture Notes of the 40^{th} Spring School organized by the Institute of Solid State Research of the Forschungszentrum Julich*, 10:1866–1807, 2009.

[7] A. D. Kent and D. C. Worledge. A new spin on magnetic memories. *Nature Nanotechnology*, 10:187–191, 2015.

[8] C. Chappert, A. Fert, and F. N. Van Dau. The emergence of spin electronics in data storage. *Nature materials*, 6:813–823, 2007.

[9] K. Peiponen, J. A. Zeitler, and M. Kuwata-Gonokami. *Terahertz Spectroscopy and Imagining.* 171. Springer Series in Optical Science, 2013.

[10] S. L. Dexheimer. *Terahertz Spectroscopy principles and applications.* CRC Press, New York, 2008.

[11] T. Seifert, N. M. Tran, O. Gueckstock, S. M. Rouzegar, L. Nadvornik, S. Jaiswal, G. Jakob, V. V. Temnov, M. Münzenberg, M. Wolf, M. Kläui, and T. Kampfrath. Terahertz spectroscopy for all-optical spintronic characterization of the spin-hall-effect metals Pt, W and $Cu_{80}Ir_{20}$. *Journal of Physics D: Applied Physics*, 51:364003, 2018.

[12] T. Seifert, S. Jaiswal, U. Martens, J. Hannegan, L. Braun, P. Maldonado, F. Freimuth, A. Kronenberg, J. Henrizi, I. Radu, E. Beaurepaire, Y. Mokrousov, P. M. Oppeneer, M. Jourdan, G. Jakob, D. Turchinovich, L. M. Hayden, M. Wolf, M. Münzenberg, M. Kläui, and T. Kampfrath. Efficient metallic spintronic emitters of ultrabroadband terahertz radiation. *Nature Photonics*, 10:483–490, 2016.

[13] Sadamichi Maekawa. Magnons, spin current and spin seebeck effect. *Bulletin of the American Physical Society*, 57, 2012.

[14] J. Sinova, S. O. Valenzuela, J. Wunderlich, C. H. Back, and T. Jungwirth. Spin hall effects. *American Physical Society: Reviews of Modern Physics*, 87, 2015.

[15] R. Rouzegar, L. Brandt, L. Nadvornik, D.A. Reiss, A.L. Chekhov, O. Gueckstock, C. In, M. Wolf, T.S. Seifert, P.W. Brouwer, G. Woltersdorf, and T. Kampfrath. Laser-induced terahertz spin transport in magnetic nanostructures arises from the same force as ultrafast demagnetization. *ArXiv: 2103.11710*, 2021.

[16] J. Jechumtál. *Studium terahertzového záření emitovaného pomocí spintronických jevů (Bachelor Thesis).* Charles univeristy, Faculty of Mathematics and Physics, 2020.

[17] Y. H. Zhu, B. Hillebrands, and H. C. Schneider. Signal propagation in time-dependent spin transport. *Phys. Rev. B*, 78:054429, 2008.

[18] L. Nádvorník, M. Borchert, L. Brandt, R. Schlitz, K. A. de Mare, Gerhard Jakob Matthias Kläui Sebastian T. B. Goennenwein Martin Wolf Georg Woltersdorf K. Výborný, Ingrid Mertig, and Tobias Kampfrath. Broadband terahertz probes of anisotropic magnetoresistance disentangle extrinsic and intrinsic contributions. *Phys. Rev. X*, 11:021030, 2021.

[19] F. L. Zeng, Z. Y. Ren, Y. Li, J. Y. Zeng, M. W. Jia, J. Miao, A. Hoffmann, W. Zhang, Y. Z. Wu, and Z. Yuan. Intrinsic mechanism for anisotropic magnetoresistance and experimental confirmation in $\mathrm{Co}_x\mathrm{Fe}_{1-x}$ single-crystal films. *Phys. Rev. Lett.*, 125:097201, 2020.

[20] F. Meier and B. P. Zakharchenya. *Optical orientation.* Sole distributors for the U.S.A. and Canada: Elsevier Science Pub. Co, Amsterdam; New York, 1984.

[21] J. Fabian, A. Matos-Abiague, C. Ertler, P. Stano, and I. Žutić. Semiconductor spintronics. *Acta Physica Slovaca*, 57:565, 2007.

[22] F. Jedema, A Filip, and B. van Wees. Electrical spin injection and accumulation at room temperature in an all-metal mesoscopic spin. *Nature*, 410:345–348, 2001.

[23] T. Jungwirth, J. Wunderlich, and K. Olejník. Spin hall effect devices. *Nature Mater.*, 11:382, 2012.

[24] I. Žutić, J. Fabian, and S. Das Sarma. Spintronics: Fundamentals and applications. *Rev. Mod. Phys.*, 76:323, 2004.

[25] Mikhail I. Dyakonov. *Spin Physics in Semiconductors.* 1. Springer, Verlag Berlin Heidelberg, 2008.

[26] C. Kittel. *Introduction to Solid State Physics.* 8^{th} Edition. Wiley, United States of America, 2005.

[27] P. Jiménez-Cavero, O. Gueckstock, L. Nádvorník, I. Lucas, T. S. Seifert, M. Wolf, R. Rouzegar, P. W. Brouwer, S. Becker, G. Jakob, M. Kläui, C. Guo, C. Wan, X. Han, Z. Jin, H. Zhao, D. Wu, L. Morellón, and T. Kampfrath. Transition of laser-induced terahertz spin currents from torque- to conduction-electron-mediated transport. *ArXiv: 2110.05462*, 2021.

[28] O. Gueckstock, L. Nádvorník, M. Gradhand, T. S. Seifert, G. Bierhance, R. Rouzegar, M. Wolf, M. Vafaee, J. Cramer, M. A. Syskaki, G. Woltersdorf, I. Mertig, G. Jakob, M. Kläui, and T. Kampfrath. Terahertz spin-to-charge conversion by interfacial skew scattering in metallic bilayers. *Adv. Mater.*, 33:2006281, 2021.

[29] T. S. Seifert, U. Martens, F. Radu, M. Ribow, M. Berritta, L. Nádvorník, R. Starke, T. Jungwirth, M. Wolf, I. Radu, M. Münzenberg, P. M. Oppeneer, G. Woltersdorf, and T. Kampfrath. Frequency-independent terahertz anomalous hall effect in $DyCo_5$, $Co_{32}Fe_{68}$, and $Gd_{27}Fe_{73}$ thin films from DC to 40 THz. *Adv. Mater.*, 33:2007398, 2021.

[30] C. v. K. Schmising, B. Pfau, M. Schneider, C. M. Günther, M. Giovannella, J. Perron, B. Vodungbo, L. Müller, F. Capotondi, E. Pedersoli, N. Mahne, J. Lüning, and S. Eisebitt. Imaging ultrafast demagnetization dynamics after a spatially localized optical excitation. *Phys Rev Let*, 112:217203, 2014.

[31] G. P. Zhang and W. Hübner. Laser-induced ultrafast demagnetization in ferromagnetic metals. *Phys. Rev. Lett.*, 85:3025, 2000.

[32] E. Beaurepaire, J. C. Merle, A. Daunois, and J. Y. Bigot. Ultrafast spin dynamics in ferromagnetic nickel. *Phys. Rev. Lett.*, 76:4250–4253, 1996.

[33] B. Koopmans, G. Malinowski, F. Dalla Longa, D. Steiauf, M. Fähnle, T. Roth, M. Cinchetti, and M. Aeschlimann. Explaining the paradoxical diversity of ultrafast laser-induced demagnetization. *Nat Mater.*, 9:259–65, 2010.

[34] G. Torosyan, S. Keller, L. Scheuer, R. Beigang, and E. T. Papaioannou. Optimized spintronic terahertz emitters based on epitaxial grown Fe/Pt layer structures. *Sci Rep*, 8:1311, 2018.

[35] O. Gueckstock, R. L. Seeger, T. S. Seifert, S. Auffret, S. Gambarelli, J. N. Kirchhof, K. I. Bolotin, V. Baltz, T. Kampfrath, and L. Nádvorník. Impact of gigahertz and terahertz transport regimes on spin propagation and conversion in the antiferromagnet irmn. *Appl. Phys. Lett.*, 120:062408, 2022.

[36] N. W. Ashcroft and N. D. Mermin. *Solid state physics.* Holt, Rinehart and Winston, New York, 1976.

[37] T. Heinzel. *Mesoscopic Electronics in Solid State Nanostructures.* 1^{st} Edition. Wiley, United States of America, 2006.

[38] A. Hirohata, K. Yamada, Y. Nakatani, I.-L. Prejbeanu, B. Diény, P. Pirro, and B. Hillebrands. Review on spintronics: Principles and device applications. *Journal of Magnetism and Magnetic Materials*, 509:166711, 2020.

[39] T. McGuire and R. Potter. Anisotropic magnetoresistance in ferromagnetic 3d alloys. *IEEE Trans. Magn.*, 11:1018, 1975.

[40] J.-H. Park, H.-W. Ko, J.-M. Kim, J. Park, S.-Y. Park, Y. Jo, B.-G. Park, S. K. Kim, K.-J. Lee, and K.-J. Kim. Temperature dependence of intrinsic and extrinsic contributions to anisotropic magnetoresistance. *Sci. Rep.*, 11:20884, 2021.

[41] P. Nam Hai, D. Sasaki, L. D. Anh, and M. Tanaka. Crystalline anisotropic magnetoresistance with two-fold and eight-fold symmetry in (In,Fe)As ferromagnetic semiconductor. *Appl. Phys. Lett.*, 100:262409, 2012.

[42] A. W. Rushforth, K. Výborný, C. S. King, K. W. Edmonds, R. P. Campion, C. T. Foxon, J. Wunderlich, A. C. Irvine, P. Vašek, V. Novák, K. Olejník, J. Sinova, T. Jungwirth, and B. L. Gallagher. Anisotropic magnetoresistance components in (Ga,Mn)As. *Appl. Phys. Lett.*, 99:147207, 2007.

[43] T. Hupfauer, A. Matos-Abiague, M. Gmitra, F. Schiller, J. Loher, D. Bougeard, C. H. Back, J. Fabian, and D. Weiss. Emergence of spin–orbit fields in magnetotransport of quasi-two-dimensional iron on gallium arsenide. *Nat Commun*, 6:7374, 2015.

[44] E. Hecht. *Optics.* 2^{nd} Edition. Addison-Wesley, Boston, 2010.

[45] F. L. Pedrotti, L. M. Pedrotti, and L. S. Pedrotti. *Introduction to Optics.* 3^{rd} Edition. Prentice Hall, New Jersey, 2007.

[46] C. Riek, D. V. Seletskiy, A. S. Moskalenko, J. F. Schmidt, P. Krauspe, S. Eckart, S. Eggert, G. Burkard, and A. Leitenstorfer. Direct sampling of electric-field vacuum fluctuations. *Science*, 350:420, 2015.

[47] M. Tinkham. Energy gap interpretation of experiments on infrared transmission through superconducting films. *Physical Review*, 104:845, 1956.

[48] J. Masi. Overview of halbach magnets and their applications. *Electrical Manufacturing and Coil Winding Expo 2010-2013*, pages 134–139, 2013.

[49] K. Seshan. *Handbook of Thin-Film Deposition Processes and Techniques: Principles, Methods, Equipment, and Applications.* Noyes Publications, 2^{nd} edition, Norwich, N.Y, 2002.

[50] Y.-S. Lee. *Principles of Terahertz Science and Technology.* Springer, New York, 2009.

[51] Mathworks, helpdesk with description of function ”smoothdata”. *https://www.mathworks.com/help/matlab/ref/smoothdata.html*, 4.4.2022.

[52] P. Kubaščík. *Study of spintronic phenomena in magnetically ordered stuctures using terahertz spectroscopy (Diploma Thesis).* Charles univeristy, Faculty of Mathematics and Physics, 2021.

[53] D. M. Nenno, L. Scheuer, D. Sokoluk, S. Keller, G. Torosyan, A. Brodyanski, J. Lösch, M. Battiato, M. Rahm, R. H. Binder, H. C. Schneider, R. Beigang, and E. Th. Papaioannou. Modification of spintronic terahertz emitter performance through defect engineering. *Sci Rep*, 9:13348, 2019.

[54] L. Šmejkal, J. Sinova, and T. Jungwirth. Altermagnetism: spin-momentum locked phase protected by non-relativistic symmetries. *ArXiv: 2105.05820*, 2021.

List of Figures

1.1 Schéma fungování SHE a ISHE 7
1.2 Scheme of spintronic emitter operation, taken from [12] 8
1.3 Scheme of ultrafast demagnetization proces 10
1.4 Defining figure of angles for AMR symmetries 15
1.5 AMR measured in CoFe by Zeng *et al.* [19] 17

2.1 Scheme of the setup in Berlin laboratory 18
2.2 Waveforms and their prectra measured in Berlin and in Prague . . 20
2.3 Scheme of operation of the electro-optical sampling, taken from [46] 22
2.4 Photo of Halbach rotator and its magnitic fields measured by hall sond 25
2.5 Schematic picture of samples used for measurement of speed of spin polarized electron transport 26
2.6 Photo of Sample 1 and 2 with labels 27
2.7 Schematical picture of Gaussian beam propagation. 29

3.1 Measured absorbed optical power on samples 1 and 2 31
3.2 Absorbance of sample 1 and 2 fitted by polynomial function . . . 32
3.3 Overview on the process of evaluation of conductance of sample 2 33
3.4 Measured and fitted conductivities of sample 2 at different places with different thicknesses of copper wedge 34
3.5 Measurement of amplitudes of THz waveforms emitted from copper wedges 36
3.6 Amplitudes of THz waveforms emitted from samples 1 and 2 normalized for calculation of spin relaxation lengths 37
3.7 Amplitudes of THz waveforms emitted from sample 1 normalized for calculation of spin current relaxation lengths with different models of absorbance and conductance 39
3.8 Observed time shifts in waveforms emitted from sample 1 ad 2 normalized on maximal value 40
3.9 Step by step demonstration of reconstruction of timeshifts from Fourier's phase 41
3.10 Times shifts evaluated on both samples by all 4 methods 42
3.11 Timeshifts evaluated by the two best methods fitted by the linear function on the area of stable copper gradient 42
3.12 Timeshifts averaged from two best methods on both samples as a function of copper thickness, fitted by a linear function in the area of stable copper gradient. 43
3.13 Scheme for estimate of the shift of the sample in z direction and the optical path which must be tranversed by THz radiation from emission to dection 45
3.14 Maximal possible change of Gouy phase and caused timeshifts of THz waveforms at the position of detection 46
3.15 Waveforms emitted from sample 1 from CoBeB(2)/Pt(2) only and its shifts evaluated from phase 47

3.16 Conductance of sample 2 measured for $d_{Cu} \approx 11.5$ nm, together with calculated curves from the Drude model for several relaxation times τ. 48
3.17 Normalized spectra of THz signals emitted from sample 1 and 2 . 49
3.18 Summary figures describing properties of spectral filtering in copper 50
3.19 Modulation of THz transmitance through sample 3 as a function of the angle α 52
3.20 First measurement of cross-crystalline AMR on CoFe 53
3.21 Improved measurement of cross-crystalline AMR on CoFe 54
3.22 Steps of evaluation of AMR with spectral resolution and resulting AMR for three orientations of sample 56